

Precisely Tuneable Temperature Modulations in Nanopores: a Novel Approach for Controllable Single-Molecule Detection

Micol Damiani

Supervisors:

Prof. Candido Fabrizio Pirri

Prof. Joshua B. Edel



**POLITECNICO
DI TORINO**

**Imperial College
London**

Master Degree in
NANOTECHNOLOGIES FOR THE ICTs
Politecnico di Torino
July 2018

Acknowledgements

First of all, I would like to thank my supervisor, Prof. Pirri, and my University, Politecnico di Torino, for giving me the possibility of developing this research project abroad, in the prestigious institution of the Imperial College London.

I would then like to express my most sincere thanks to my supervisor at Imperial College London, Prof. Joshua Edel, and Dr. Alex Ivanov, for the chance of working in the Edel Group, and for assigning me with this challenging project. Their expert advice and feedback during all the stages of the project were a constant source of motivation. A big thank you goes to all the members of the Edel Group, for their support, encouragement, and friendliness throughout all the months I spent at Imperial College. In particular, I would like to thank Liang Xue, for the mentoring, the support, and the advice that contributed to the development of this project, and for providing me with control data on the device fabricated. I am grateful to Dr. Paolo Cadinu and Dr. Binoy Paulose Nadappuram, for always being ready to help me and share their expertise. Thank you also to Dr. Minkyung Kang, for providing the SEM images of the pipettes, and to Dr. Leo Velleman, for the training on the Raman set-up. I would also like to thank Sonalika Jain, who worked in parallel to me on a similar project. Being able to share ideas and solve some of the problems together made everything more pleasant.

Finally, I would like to thank all of my friends, both the new ones from London and the old ones from Italy, for being a constant source of happiness, and for making me feel at home whenever I was with them. Last but not least, my biggest thank you goes to my parents and my sister, for being ever-present and supportive, through the good and the bad moments, and for always pushing me to be the best version of myself, academically and not.

Abstract

Precisely Tuneable Temperature Modulations in Nanopores: a Novel Approach for Controllable Single-Molecule Detection

Micol Damiani

Developing versatile and highly sensitive biosensing platforms is one of the major focuses of healthcare research. Rapid and accurate characterisation of single biomolecules is crucial for achieving a deep understanding of their behaviour, which will aid major advancements in disease diagnosis and treatment. Owing to their sensitivity, high-speed, high-throughput, and label-free approach, nanopores are becoming a widely used versatile tool for single-molecule detection. To unfold the full potential of nanopore systems, several challenges need to be addressed, such as achieving a precise control over the experimental conditions, and manipulating the molecular transport in the pore region. In the present work, the integration of laser optics allows the modulation of the conditions in the localised environment of the pore, by exposing a plasmonic gold nanopipette to regulated laser radiation. Due to localised heating, the resulting ionic current enhancement is used to quantify the local temperature variations, meaning that the pore can also be employed as a nanoscale thermometer. The low-noise heating is then used to manipulate the capture rate of 10 kbp DNA, and a precise control over the throughput of the system is achieved.

Table of contents

List of figures	5
List of tables	7
Nomenclature	8
1 Introduction	1
1.1 Biosensing	1
1.2 Single-Molecule Detection	2
1.3 Nanopore Sensing	2
1.3.1 Working Principle	3
1.3.2 Platforms for Nanopore Sensing	5
1.4 Nanopore Heating	8
1.4.1 Manipulating DNA Translocations	8
1.4.2 Modulating Temperature in Nanopores	9
1.4.3 Device Proposed	11
2 Project Objectives	12
3 Experimental Methods	13
3.1 Pipette Fabrication	13
3.1.1 Laser Pulling of Dual-Barrel Quartz Capillaries	13
3.1.2 Fabrication of the Carbon Electrode by Pyrolysis of Butane .	14
3.1.3 Electrodeposition of Gold onto the Carbon Electrode	15
3.1.4 Surface Characterization	16

Table of contents	4
<hr/>	
3.2 Experimental Set-Up	16
3.2.1 Electrodes and Solutions	16
3.2.2 Coverslip Set-Up	17
3.2.3 Faraday Cage	17
3.2.4 Integration of Laser Optics	18
3.3 IV and Conductivity Measurements	19
3.4 DNA Translocations and Data Analysis	19
3.4.1 DNA Translocations	19
3.4.2 Data Analysis	20
4 Results and Discussion	21
4.1 Pipette Fabrication	21
4.1.1 Gold Electrodeposition	22
4.1.2 Characterization of Modified Pipette	24
4.2 Local Temperature Modulation	26
4.2.1 Integrating Laser Heating with Nanopore	26
4.2.2 IV and Conductance Modulation	29
4.2.3 Temperature Conversion	31
4.2.4 Stability of the System	32
4.3 Controlling Single-Molecule DNA Translocations	35
4.3.1 DNA Translocations through Plain and Gold Pipettes	35
4.3.2 Modulating DNA Translocations by Precisely Tuning the Local Temperature	37
4.4 Mechanism behind Capture Rate Enhancement	45
5 Conclusion	47
6 Future Research	48
References	49

List of figures

1.1	Schematic of the current trace during a translocation event	4
1.2	Examples of biological nanopores and their applications for DNA-sequencing	6
1.3	Work-flow for the fabrication of a membrane and nanopore	7
1.4	Optical images of a nanopipette tip	8
1.5	Different structures used to induce nanopore heating	10
1.6	Schematic of the device used in the current work	11
3.1	Schematic of the laser pulling of nanopipettes	14
3.2	Schematic of the pyrolytic carbon deposition in one of the barrels of the pipette	14
3.3	Schematic of the electrodeposition of gold on the tip of the carbon electrode	15
3.4	Customised coverslip set-up	17
3.5	Customised electrical detection set-up integrated with laser optics to enable temperature modulations	18
3.6	Protocols used for IV measurements	19
3.7	Basic schematic of a DNA translocation experiment on a AuDBNP	20
4.1	Characterisation of the fabricated dual-barrel nanopipettes, before and after pyrolytic carbon deposition	22
4.2	Current traces associated to the gold deposition process	23
4.3	Examples of current traces associated to the gold deposition process	25
4.4	Characterisation of the fabricated pipettes after Au deposition	26

4.5	Comparison of the noise levels associated to laser irradiation, for two different laser wavelengths	28
4.6	Effects of the laser induced-local heating on the ionic current	30
4.7	Instantaneous and reversible changes induced by laser illumination on the AuDBNP	30
4.8	Linear fitting of the conductivity of bulk KCl	32
4.9	Temperature changes associated to laser exposure and pipette's conductance as a function of temperature	32
4.10	Stability of the system	34
4.11	Example of the results obtained from a voltage-dependent translocation study on a plain dual-barrel nanopipette	36
4.12	Control experiments on a C-DBNP, confirming the negligible effects of laser exposure on DNA translocations	37
4.13	Schematic of the two strategies used to investigate the effects of localised temperature modulation on the DNA translocations	38
4.14	Results illustrating the temperature-induced effects on DNA translocations, using Strategy 1	40
4.15	Results illustrating the detailed temperature-induced effects on the translocation dynamics	42
4.16	Summary of the results of the temperature-induced effects on DNA translocation	43
4.17	Summary of the preliminary results of the effects of pulsed laser exposure on DNA translocations	44

List of tables

1.1	Comparison of the main properties of three types of nanopores . . .	5
3.1	Parameters used in the laser puller program	14

Nomenclature

Roman Symbols

$\alpha - HL$	Alpha-hemolysin
δt	Inter-event Time
<i>ALD</i>	Atomic Layer Deposition
<i>AuDBNP</i>	Gold-Deposited Dual-Barrel Nanopipette
<i>C - DBNP</i>	Carbon-Deposited Dual Barrel Nanopipette
<i>DDL</i>	Diffusive Double Layer
<i>DI</i>	Deionised
<i>EBL</i>	Electron Beam Lithography
<i>FIB</i>	Focused Ion Beam
<i>FWHM</i>	Full-Width Half Maximum
<i>I - t</i>	Current-Time
<i>I.D.</i>	Inner Diameter
I_0	Open-Pore Current or Baseline Current
I_B	Blockade Current or Peak Current
<i>IV</i>	Current-Voltage
<i>kbp</i>	kilo-base pair
<i>LPCVD</i>	Low-Pressure Chemical Vapour Deposition
<i>MspA</i>	Mycobacteriumsmegmatis porin A
<i>O.D.</i>	Outer Diameter

<i>PSD</i>	Power Spectrum Density
<i>R_C</i>	Capture Rate
<i>RE</i>	Reference Electrode
<i>SERS</i>	Surface-Enhanced Raman Spectroscopy
<i>SMD</i>	Single-Molecule Detection
<i>STD</i>	Standard Deviation
<i>t_d</i>	Dwell Time
<i>TEM</i>	Transmission Electron Microscopy
<i>WE</i>	Working Electrode

Chapter 1

Introduction

1.1 Biosensing

Biosensors are devices which combine a biological responsive element with a chemical or physical transducer, allowing for the selective and quantitative detection of a specific analyte among a wide range of compounds. In particular, the signal generated by the interaction between the analyte and the biological element, which can be optical, electrical, or mechanical, is amplified and measured by an electronic or optical system [1]. Biosensors' merits lie in their capability of delivering complex bioanalytical measurements in simple formats, with fast response time (which can range from milliseconds to a few minutes), while maintaining high specificity. Therefore, they offer an ample variety of applications, such as medical diagnostics, food safety, and environmental screening [2]. The integration of biosensors with semiconductor technologies paved the way for miniaturization, which allowed the fabrication of portable devices, capable of probing nanoscale analytes [3].

Conventional commercial diagnostic methods, such as enzyme-linked immunosorbent assay (ELISA) and polymerase chain reaction (PCR), involve biochemical approaches, and are time-consuming, expensive, and present a limited accuracy [4]. As a consequence, achieving sensors with faster response times, lower detection limits, point-of-care use, and a higher specificity is desirable. Therefore, over the last decades, healthcare research has been focusing on how to develop biosensors capable of improving the field of medical diagnostic and disease treatment.

For example, early detection is a key factor in preventing and/or successfully treating certain kinds of diseases, like cancer, and this requires the detection of specific proteins at very low concentrations. At the earliest stage of illness, when

external symptoms are not manifested yet, cancerous tissues already produce particular proteins, called biomarkers, altering their concentration in serum. Being able to measure these changes with high specificity is crucial for early stage diagnosis, and consequently for a successful treatment [5]. Thanks to their specificity and to the ability to probe micro and nano-scale analytes, biosensors are playing a key role in diagnostics [5–7]. In addition to this, other potential applications include investigating genetic mutations [8, 9], and identification of pathogens related to infectious diseases [10, 11].

1.2 Single-Molecule Detection

An intrinsic limitation of conventional biosensors is that they measure the ensemble average of a sample, resulting in masking and loss of rare events and details about individual biomolecules. Single-molecule analysis is a feasible way to further characterise complex biological systems, composed by heterogeneous mixtures [12, 13]. Having techniques capable of revealing heterogeneities and stochastic processes within biological systems and their interactions, will lead to a deeper understanding of their behaviour. In turn, this will promote dramatic advancements in the above-mentioned fields of medical diagnosis and drug design. Moreover, the development of single-molecule detection (SMD) techniques paves the way for DNA sequencing, crucial in the understanding of disease, inheritance, and individuality [14].

To date, a diversity of techniques that enable SMD has been researched, including fluorescence spectroscopy [15, 16], total internal reflection spectroscopy [17–19], surface-enhanced Raman spectroscopy (SERS) [20–22], optical tweezers [23, 24], and atomic force spectroscopy [25–27]. Although promising, the development of novel methods for single-molecule detection takes a leap forward for better achieving the necessities of healthcare. [2].

Over the past decade, nanopore technology has been playing an increasingly emerging role in SMD and biosensing, offering the possibility of performing fast, high-throughput, cost-effective, and label-free detection of a variety of analytes and biomolecules [28, 29].

1.3 Nanopore Sensing

Nanopores first emerged as a potential biosensing platform when Kasianowicz *et al.* [30] demonstrated that it was possible to electrophoretically drive single-stranded

DNA (ssDNA) and RNA through a 2.6 nm pore in a lipid bilayer membrane. Since then, scientific research has been investigating the improvement of the functionalities and applications of nanopores in SMD. Their attractiveness lies in the simplicity of the detection mechanism and on the fact that it is a low-cost, label-free, amplification free, single-molecule approach that requires low reagent volumes [14].

Up to now, nanopore-based sensing has been applied to the study of biopolymers, such as DNA and RNA [31, 32], antibody binding kinetics [33], monitoring protein-DNA interactions [34], and detecting low-concentration proteins in human serum [5]. In addition to this, nanopore technology has emerged as a tool for high-throughput and label-free DNA sequencing [14, 28, 35–37], capable of overcoming the limitations of previous generation sequencing methods (Sanger and pyrosequencing approaches [38, 39]), which require amplification and labelling of DNA, and exhibit a lower sensitivity and speed.

1.3.1 Working Principle

A nanopore is a nanoscale aperture, having a diameter smaller than 100 nm, formed in an insulating membrane, which separates two chambers filled with a solution containing an electrolyte (usually KCl) and the analyte of interest.

When a voltage is applied between the two chambers through non-polarisable electrodes (usually made of Ag/AgCl), the exchange of ions from one side of the membrane to the other generates a steady state current, named open-pore current I_0 . More in detail, the AgCl oxidation at the anode removes Cl^- ions from the solution, while, at the cathode, the inverse reduction releases Cl^- . For applied biases between -1 V and +1 V, the current-voltage response of the nanopore is Ohmic, and it depends on the electrolyte's ionic strength and on pore geometry [28].

Charged biopolymers, such as DNA and RNA, are driven through the pore by the applied voltage, and the transport of the molecule through the pore, called translocation, temporarily modulates the current flow, producing an ionic-current blockade I_B , as shown in Figure 1.1a. The amplitude, duration and shape of the blockade provide useful information about the target analyte, such as size and structure, and its interactions with the pore. In general, translocation events are determined by an interplay between electrophoresis, electroosmosis, and diffusion, and additionally influenced by physical factors, such as surface charges, solution viscosity and ion mobility [3, 29].

The translocation process can be characterised by several key parameters, as depicted in Figure 1.1b:

- **Blockade current I_B** , (referred to as peak current as well) typically between 1 pA - 10 nA;
- **Dwell time t_d** : the amount of time the molecule spends inside the pore, typically between 1 μ s - 10^{-1} s;
- **Inter-event time δt** : the waiting time between two successive events, related to the **capture rate R_C** , which is the number of events per unit time.

As mentioned before, by analysing these parameters it is possible to retrieve information about the structure, the size and the interactions of the translocating molecule.

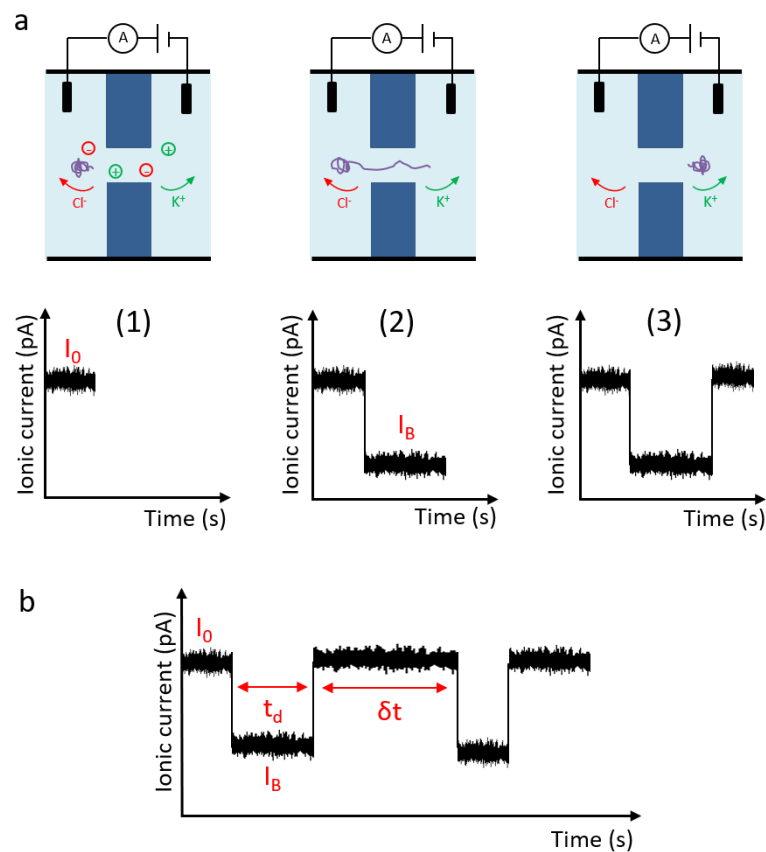


Fig. 1.1 Schematic of the current trace during a translocation event: (a) The three consecutive stages of a typical nanopore measurement. (1) The applied voltage induces the flow of the open pore current, I_0 , monitored in real time. (2) As the charged analyte translocates, it partially blocks the volume of the pore, resulting in a current modulation, I_B . (3) After the translocation, the current returns to its original value I_0 . (b) Parameters characterising a translocation event: current blockade I_B , dwell time t_d , inter-event time δt .

1.3.2 Platforms for Nanopore Sensing

A large diversity of nanopores exists, characterised by a variety of structures, geometries and materials. The most common types can be grouped into two broad categories, according to the material used to assemble them: biological and solid-state nanopores. Nanopipettes, which are employed in the current study, are a specific type of solid-state nanopore. The main differences between these three platforms are highlighted in Table 1.1

	Biological	Solid-state	Nanopipettes
Material	Pore-forming proteins embedded in a lipid-bilayer membrane	SiN_x , SiO_2 , metal oxides, graphene	Borosilicate glass or quartz
Fabrication	Natural self-assembly of proteins	Multi-step method involving photolithography, FIB or EBL milling	Laser pulling of glass/quartz capillaries
Pore size	Limited by the pore forming proteins, 1.4 nm for $\alpha - HL$ and 1.2 nm for MspA	Controllable between 2-100 nm	Controllable between 10-100 nm
Surface modification	Possible by site-specific mutagenesis	Possible via a wide range of surface chemistries	Similar to solid-state nanopores

Table 1.1 Comparison of the main properties of three types of nanopores

Biological Nanopores

Biological nanopores, inspired by the ones found in nature, consist of a pore embedded in a lipid bilayer, and offer a number of advantages for single-molecule DNA analysis respect to their solid-state counterpart. Owing to their highly controllable and reproducible pore geometry and high spatial resolution, the most commonly used biological nanopores, *alpha-hemolysin* ($\alpha - HL$) and *Mycobacteriumsmegmatis porin A* (MspA), shown in Figure 1.2a, have shown superior capabilities in SMD of DNA, including the identification of the four nucleotides, Figure 1.2b [37, 40–44].

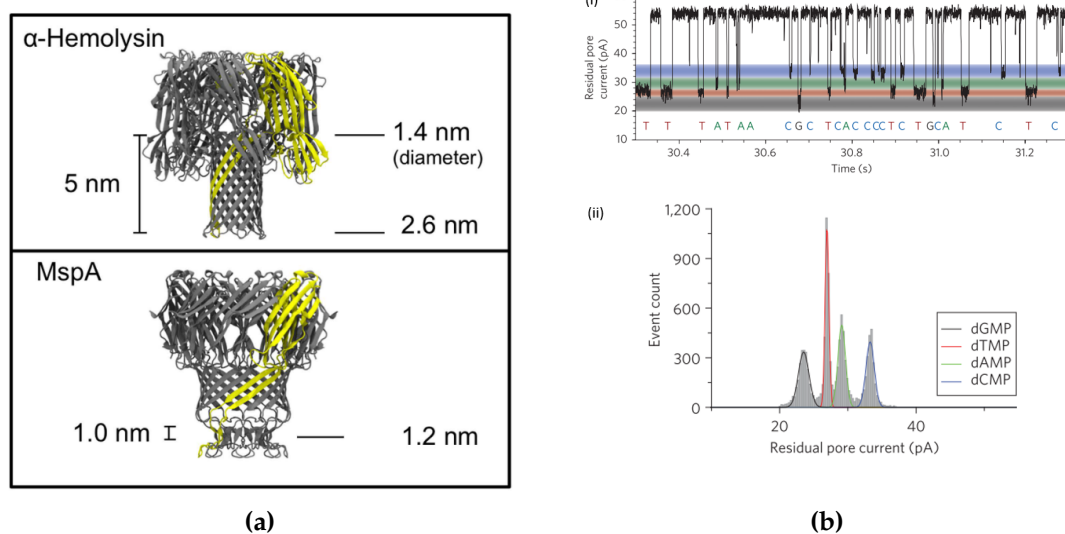


Fig. 1.2 Examples of biological nanopores and their applications for DNA-sequencing: (a) α -HL, a protein with 1.4 nm and 2.6 nm constrictions, and MspA, a protein with a single 1.2 nm pore [37]. (b)(i) A current-time trace for DNA translocations through a modified α -HL pore, showing the discrimination between the 4 nucleotides, and (ii) the distribution of ionic current signals relative to each of the four bases (A, T, G, C) [44].

However, biological nanopores present inherent disadvantages, which make their application challenging. These include the chemical instability of the lipid bilayer, the sensitivity to experimental conditions, such as temperature, pH, salt concentration, and the difficulty of integration in large-scale arrays [14]. Moreover, the limited range of pore sizes available reduces the class of examinable analytes to ssDNA and small molecules.

Solid-State Nanopores

Synthetic nanopores, fabricated in solid-state materials, have proven to be a valid versatile alternative to biological pores. Characterised by a superior mechanical robustness, and chemical and thermal stability, their advantages lie in the ability to tune the size and shape of the pore with sub-nanometre precision, achieved by the integration of fabrication techniques typical of semiconductor technology. Moreover, the solid-state approach enables the fabrication of high-density arrays of nanopores, which are also compatible with various electronic and optical measurement techniques, as well as microfluidic systems [14, 41, 45–47].

An additional key strength of solid-state nanopores is given by the possibility of pairing or replacing the more conventional electrical detection with novel alternative techniques, in order to increase the amount of information about the

analyte extracted. These include optical detection [48, 49], electron tunnelling [50] and magnetic tweezers [51].

Due to its high mechanical stability, low stress, and good insulating properties, Silicon Nitride (SiN_x) has been the most commonly used pore membrane material, supported on a silicon wafer. Other typical materials used include, among others, SiO_2 [52], SiC [53], metal oxides [54], and graphene [55]. The free standing SiN_x membranes are fabricated on silicon wafers using a standard photolithographic process, as depicted in Figure 1.3a. To incorporate the pore in the membrane, the most used techniques include electron-beam lithography (EBL), transmission electron microscopes (TEM), which allow to obtain pores with diameters between 1-10 nm, and focused ion-beam milling (FIB), more versatile in terms of materials and dimensions, depending on the ion source used (typically Ga^+ , He^+ , Ne^+) [3].

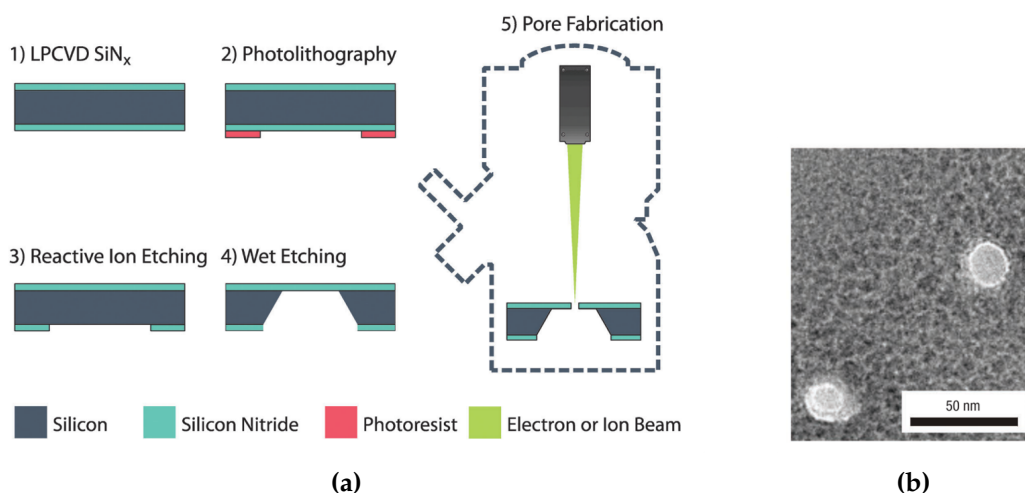


Fig. 1.3 Work-flow for the fabrication of a membrane and nanopore: (a) the steps of the photolithographic process used to fabricate a SiN_x membrane, and the fabrication of the pore through EBL or FIB [3]. (b) TEM micrograph of a membrane where two pores were drilled by a finely focused electron beam inside a TEM microscope [52].

After fabrication, a number of surface-modification techniques can be employed to further improve the nanopore in terms of selectivity and sensitivity. These include atomic layer deposition (ALD) [54, 56], surface functionalisation [57, 58], and electrodeposition [59, 60].

The major drawback related to solid-state nanopores is their fabrication, which is complex, long and expensive, reducing the efficiency and throughput [41]. To address these issues, an appealing alternative is given by quartz/borosilicate nanopipettes, as a result of their quick, reliable and inexpensive fabrication [47].

Nanopipettes

Nanopipettes, a sub-class of solid-state nanopores, are fabricated from glass or quartz capillaries, through mechanical laser-assisted pulling, which produces exceptionally sharp tips with high aspect ratio. By controlling the pulling parameters, it is possible to tune the pipette's geometry, obtaining different taper lengths and pore diameters, which usually range between 10 nm and several hundreds of nanometres [29, 61]. As well as being inexpensive and easy to fabricate, as specified above, nanopipettes exhibit also a high electrical and chemical stability [62].

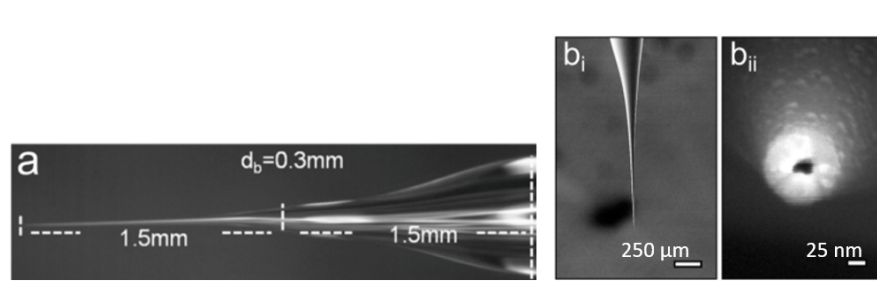


Fig. 1.4 Optical images of a nanopipette tip: (a) Optical micrograph showing the dimensions of the tip, shank, and shoulder [47]. (b) SEM images of the nanopipette (b)(i) tip and (b)(ii) pore size [63].

Pore sizes can be reduced by surface modifications [56, 64], and additional features can be integrated with the nanopipette, to improve and expand the detection mechanism. For example, it is possible to position pipettes into microfluidic channels, for in-flow DNA detection [47], to apply dielectrophoretic trapping at the tip [65], or to integrate the detection with SERS [21].

Additional functionalities can be obtained by using dual-pore capillaries, which, when pulled, give rise to two adjacent nanopores, separated by a 20-nm gap [66]. The presence of two independently addressable pores paves the way for a vast range of applications and modifications that improve the performances of the standard one-pore detection mechanism [67–69].

1.4 Nanopore Heating

1.4.1 Manipulating DNA Translocations

The ability to control the local environment of the pore and to manipulate the translocation dynamics is crucial to the refinement of the detection accuracy and throughput of sensing devices. Perturbing the analyte and the local conditions

during translocation, produces a variation in the recorded signal, which can provide a greater insight into the properties of the analyte molecule [70]. Concerning DNA experiments, it would be desirable to address singular properties, such as translocation speed or capture rate, without degrading the current signal and the signal-to-noise ratio (SNR).

Manipulating translocations can be achieved by using either a chemical or a physical approach. The first one includes chemically modifying the nanopore's surface or the analyte itself, through specific functionalisation, in order to activate distinct interactions between the two [71–73]. Physical manipulation consists in varying, for example, the voltage, to induce dielectrophoretic trapping [65], or the buffer viscosity [74], or introducing salt gradients [75–77], or pressure gradients [78], which allow to achieve control on translocation speed and throughput. Alternatively, temperature modulations have proven to be a versatile tool to achieve control over DNA translocations.

1.4.2 Modulating Temperature in Nanopores

The ability to modulate temperature allows to achieve control over the nanopore without the need for complex chemical modifications. In turn, this provides the means for investigating the behaviour of an analyte in a heated environment and achieving control over its motion. In addition to this, understanding how the nanopore's characteristics depend on heating will enable to use the pore as a nanoscale temperature probe [79]. Therefore, efforts in optimising temperature modulations are directed towards the achievement of an improved targeted heat absorption and a maximised control over DNA translocations [80].

Nanopore temperature modulations can be attained by generalised bulk heating of the pore and surrounding environment, which is usually slow and less efficient, or by targeted heating, which requires the addition of specific surface features [70]. Owing to their superior properties, plasmonic nanostructures have recently become the most common surface modification used to induce local heating. These metallic nanostructures selectively absorb radiation through the excitation of collective electron oscillations, called surface plasmons. When plasmons decay, the non-radiative absorption results in local heating and a temperature increase around the nanopore [81]. Therefore, the integration of laser optics with metallic nanostructures has been meticulously explored, both theoretically and experimentally, to investigate plasmonic applications in nanopore heating.

Gold is the most popular material used for integrating plasmonic nanostructures around the pore, as it is efficient in both heat generation and dissipation,

due to its high thermal conductivity [70]. Over the years, a number of different structures have been implemented, such as bowtie antennas [81–83] and bullseye structures [70, 80], as reported in Figures 1.5a and 1.5b.

Nicoli *et al.* investigated the effects of laser-induced local heating by integrating a plasmonic gold bowtie antenna at the entrance of a SiN_x pore [81]. As it can be seen from Figure 1.5a(ii), the absorption cross-section of the structure is maximised at a specific wavelength, and by exciting the structure with such radiation, the resulting heating is extremely localised. This produces an increase of current and event rate, Figure 1.5a(iii), and an increase of conductance blockade, Figure 1.5a(iv).

Crick *et al.* implemented a device consisting of a Au-bullseye structure with specific ring periodicity surrounding the pore, depicted in Figure 1.5b(i) [70, 80]. Depending on the wavelength used for excitation, the electric field enhancement, and the related temperature increase, were more pronounced, Figures 1.5b(ii) and 1.5b(iii). Moreover, as reported in Figure 1.5b(iv), a decrease in dwell time and an increase in peak current were observed.

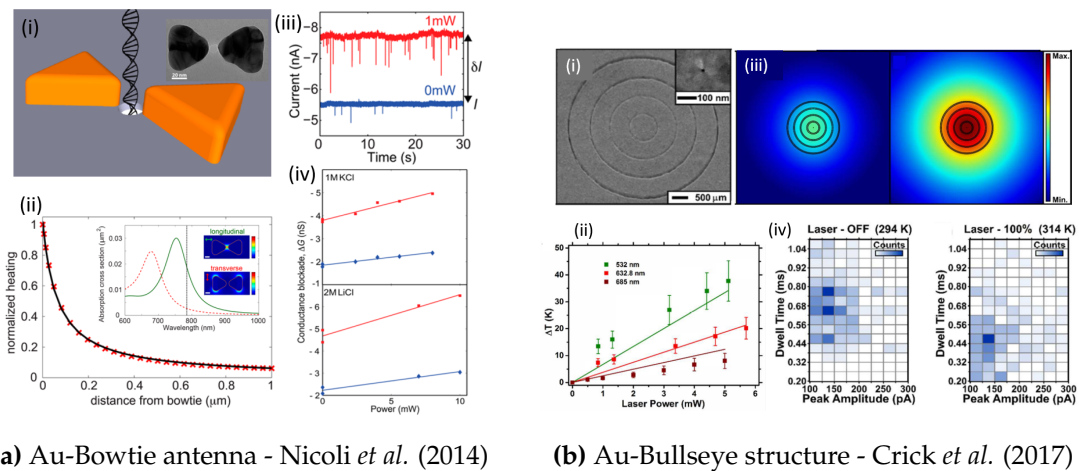


Fig. 1.5 Different structures used to induce nanopore heating. (a) Au-bowtie antenna: (i) Schematic of a DNA molecule translocating through the fabricated plasmonic nanopore and (inset) TEM top-view image of the device. (ii) Normalized heating profile away from the nanopore, obtained from measurements (black) and simulations (red), demonstrating the localised nature of the heating. (inset) Simulated absorption cross sections of the plasmonic nanopore. (iii) Examples of current traces that illustrate the plasmon-induced event rate enhancement in 2 M LiCl. (iv) Increase of the current blockade signal in 1 M KCl and 2 M LiCl [81]. **(b) Au-bullseye:** (i) SEM images of the bullseye structure with a defined ring periodicity, and (inset) FIB image of the nanopore milled into the gold side of the free-standing membrane. (ii) Experimental (dots) and simulated (line) temperature change as a function of laser power, for 3 different wavelengths. (iii) Temperature map for 632.8 nm laser (left) and 532 nm laser (right), 5 mW. Minimum: 6K, and Maximum: 33.5K. (iv) 2D-histogram plots showing a decrease in dwell time and an increase in peak current upon laser irradiation [70].

Other examples include the work of Yamazaki *et al.*, where the photoexcitation properties of SiN_x were exploited to optically induce non radiative heating [84], and the work of Zhang *et al.*, where the combined effects of thermal and potential gradients were employed for differentiating DNA molecules with different lengths in a nanopore array [85].

1.4.3 Device Proposed

A shared result of the above mentioned works is given by the increase of electrolyte conductivity induced by temperature [79, 81, 83, 84]. However, the exact effects of localised heating on nanopore's performances and DNA translocations are still debated and strongly depend on the type of architecture used.

This work presents a novel platform aimed at achieving control over the localised environment of the nanopore and over translocation throughput. The device fabricated consists of a dual-barrel nanopipette, in which one of the barrels is filled with amorphous carbon and gold is electrodeposited at the tip. This provides a quick and easy-to-fabricate device which, upon laser exposure, is equipped with a heating element. The open barrel of the pipette is used for investigating the effects of heating on DNA translocations.

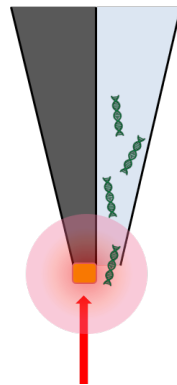


Fig. 1.6 Schematic of the device used in the current work: one of the barrels of the dual-barrel nanopipette is filled with carbon and gold is electrodeposited at the tip. Upon laser exposure the gold acts as a heater. The empty barrel is used for DNA translocations.

Chapter 2

Project Objectives

Overall, the aim of this project was to achieve precise control over the temperature in the localized environment of the nanopore, and to investigate the effects of the regulated heating on DNA translocation dynamics. More specifically, the consequences on the key parameters of dwell time, blockade current, and capture rate, which characterize a translocation event, were closely examined. Manipulating the detection through precisely tunable temperature modulations, could improve the functionalities and performances of single-molecule nanopore sensing, and provide more detailed information about the analyte.

To achieve this goal, the following objectives were set:

- Establishing a reliable experimental apparatus for controlling the local temperature at the nanopore
 - Fabricating the dual-barrel gold-deposited nanopipettes (AuDBNPs) used in the experiments
 - Setting up the system needed to integrate laser optics and electrical detection
 - Quantifying the local temperature changes induced by laser illumination at the tip of the AuDBNP
- Achieving control over DNA translocations through the localised heating
 - Establishing feasibility of DNA translocations on AuDBNPs
 - Investigating and quantifying the effects of heating on translocation dynamics

Chapter 3

Experimental Methods

All chemicals were purchased from Sigma Aldrich and, unless otherwise specified, used as received. All solutions were prepared on the day of use, with deionised (DI) water (SUEZ Water, UK) as the solvent, and filtered through 0.2 μm membrane/syringe filters (Pall Corporation) to remove any insoluble impurity. To reduce noise and interference produced by the surrounding environment, all electrical measurements were performed in a custom-built Faraday Cage. Bright and dark-field characterization of the fabricated nanopipettes was performed on an optical microscope (BX51, Olympus), while SEM imaging was performed on a Leo Gemini 1525 field emission gun scanning electron microscope. All the nanopipettes were stored in sealed petri dishes or sealed glass vials, to minimise contamination, and each pipette was used only once for different experiments.

3.1 Pipette Fabrication

3.1.1 Laser Pulling of Dual-Barrel Quartz Capillaries

Dual-barrel theta quartz capillaries (Friedrich & Dimmocck, inc.; 1.2 mm O.D. \times 0.90 mm I.D. \times 100 mm length) were cleaned inside a Plasma Cleaner (Harrick) for \sim 20 min to remove any surface impurity. Dual-barrel nanopipettes were fabricated using a laser puller (P-2000, Sutter Instruments): a laser beam with a pre-set power is focused at the centre of the capillary, inducing local heating, followed by a pulling force exerted on both sides to produce the sharp nanoscale tips, as shown in Figure 3.1. Specifically, for the current experiment, a two-step program was used, whose parameters can be found in Table 3.1. The first step created a taper at the centre of the capillary, while the second step pulled the capillary into the actual nanopipette, having a pore size of approximately 20-60

nm across each barrel. It should be noted that the pulling protocol is device-dependent and sensitive to temperature and humidity [56].

	Heat	Filament	Velocity	Delay	Pull
Line 1	870	4	30	160	100
Line 2	900	3	20	130	60

Table 3.1 Parameters used in the laser puller program

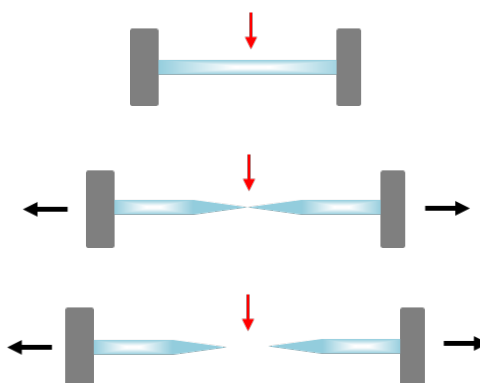


Fig. 3.1 Schematic of the laser pulling of nanopipettes: a laser beam is focused at the centre of the capillary, locally heating it, while a pulling force exerted on both sides produces the sharp tips.

3.1.2 Fabrication of the Carbon Electrode by Pyrolysis of Butane

The fabrication of the carbon electrode in one of the two barrels was performed through pyrolytic deposition, following the procedure described in [68, 69]. To ensure that the deposition happened in one barrel of the pipette only, one barrel was sealed with Blu Tack (Bostick), while butane was pumped in the other through a silicon tubing. A butane torch was used to heat the tip of the nanopipette to induce pyrolysis of butane, while an argon flow was maintained to prevent oxidation of the deposited carbon. To produce extensive and uniform filling of amorphous carbon throughout the one barrel, heating was maintained for 20s. A schematic of the set-up can be seen in Figure 3.2.

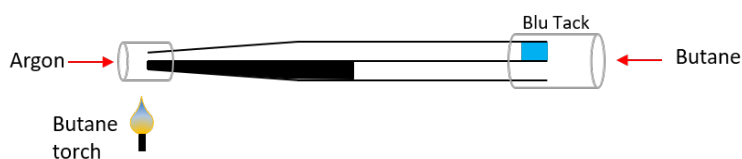


Fig. 3.2 Schematic of the pyrolytic carbon deposition in one of the barrels of the pipette

3.1.3 Electrodeposition of Gold onto the Carbon Electrode

After the fabrication of the carbon electrode, gold was deposited on the tip of the carbon-filled barrel using a biopotentiostat (CHI 760C, CH Instruments), following a modified version of the procedure proposed by Rutkowska *et al.* [59]. A schematic of the setup used is reported in Figure 3.3.

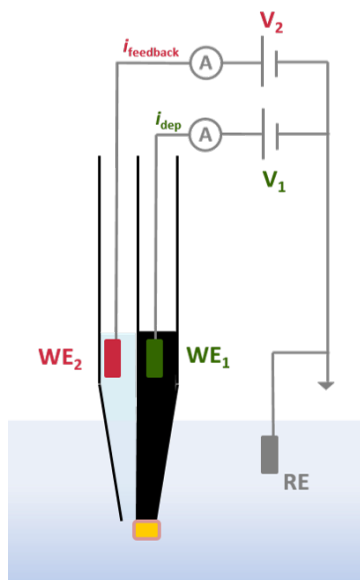
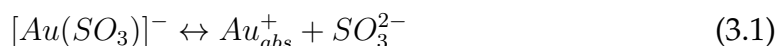


Fig. 3.3 Schematic of the electrodeposition of gold on the tip of the carbon electrode: the process is monitored by the current $i_{feedback}$ flowing in the open barrel. Working electrode 1 (WE₁): Cu; Working electrode 2 (WE₂): Ag; Reference electrode (RE): Ag.

The pipette was dipped in ECF64 gold plating solution (Metalor), which contains 44 mM of NH_4AuSO_3 in 520 mM $(\text{NH}_4)_2\text{SO}_3$. Before loading it on the deposition platform, the solution was diluted ten times with DI water. To minimise gold contamination, the un-modified open barrel of the pipette was filled with 52 mM $(\text{NH}_4)_2\text{SO}_3$. A 0.25 mm Cu wire (Goodfellow), used as first working electrode (WE₁), was inserted in the carbon-filled barrel, while a 0.125 mm Ag wire (Goodfellow) was inserted both in the open barrel, as a second working electrode (WE₂), and in the plating solution, to act as a reference electrode (RE).

A potential V_1 of -0.73 V was applied to WE₁ to induce the deposition of gold on the carbon electrode, via a two-step reduction process, which involves the dissociation of gold in the ECF64 solution, (reaction 3.1) and the consequent reduction of the absorbed gold on the carbon electrode surface (reaction 3.2)



In order to have a real-time indication of the dimensions of the open pore during the deposition, a small potential V_2 of -0.1 V was applied to WE_2 , inducing the current $i_{feedback}$. The deposition was stopped when $i_{feedback}$ showed an abrupt decrease, which indicates that gold is growing over the open pore, shrinking its dimensions. To ensure consistency in pore size between different pipettes, the deposition was stopped when $i_{feedback} = -1.5$ nA. Both the deposition current i_{dep} and the open-pore current $i_{feedback}$ were recorded at a sampling interval of 1 s.

To monitor the changes induced by gold deposition, the IV characteristic of the open barrel was recorded through cyclic voltammetry (-0.5 V - 0.5 V, scan rate 0.05 V/s, sampling interval 0.02 V) before and after the process. To reduce all external noise, this fabrication step was performed inside a Faraday cage. After the deposition, the open barrel was rinsed with DI water to remove all traces of deposition solution, which might affect further experiments, and, to avoid salt crystallization at the tip, the fabricated AuDBNPs were stored in a sealed vial filled with DI water until use.

3.1.4 Surface Characterization

The fabricated AuDBNPs were characterised using different types of microscopes. Bright and dark-field microscopy was performed on an optical microscope (BX51, Olympus), while SEM was performed on a Leo Gemini 1525 field emission gun scanning electron microscope.

To perform SEM, the freshly fabricated AuDBNPs were stored in a sealed vial filled with DI water for a few hours, to remove any trace of salt from the tip, and they were then transferred in a sealed Petri dish, where they were left to dry for a few hours. The tips were then secured on a 45°-tilted holder using carbon tape, which is conductive and extremely sticky. To improve fixing, the pipettes were also partially covered with a conductive silver paint, and left to dry overnight. Finally, the sample was transferred on the microscope's stage to perform SEM.

3.2 Experimental Set-Up

3.2.1 Electrodes and Solutions

All measurements on pipette conductivity and DNA translocations were performed using Ag/AgCl electrodes. 0.125 mm Ag wires (Goodfellow) were electroplated in a solution of 1 M KCl by applying a voltage of 2 V for 120s on the

biopotentiostat (CHI 760C, CH Instruments), while monitoring the chronoamperometric curve. At the end of the fabrication, the wires were rinsed in DI water and stored in a petri dish until use.

A stock solution of 100 mM KCl in TE buffer (pH 8) was made and stored at room temperature, and, before performing experiments, the solution was filtered. To perform translocation experiments, a 400 pM 10 kbp DNA solution was prepared by serial dilution of a stock solution (500 $\mu\text{g}/\text{mL}$ stock concentration, New England Biolabs) in 100 mM KCl in TE buffer.

3.2.2 Coverslip Set-Up

All the experiments related to local heating and laser illumination were performed assembling the fabricated pipettes on a customised coverslip set-up, as depicted in Figure 3.4. A droplet of 100 mM KCl, acting as external reservoir, was placed on a cover slip (25 x 50 x 1.5 mm, borosilicate glass, VWR) within a glue boundary (Ecoflex 5, Smooth-On). For the IV studies, KCl electrolyte was injected in the open barrel of the AuDBNP (the internal reservoir) with a Microfill needle (World Precision Instruments). For DNA translocation studies, the pipette was filled with the prepared 10 kbp DNA solution following the same procedure. The Ag/AgCl reference electrode was dipped in the KCl droplet, while the Ag/AgCl working electrode was inserted in the pipette. To ensure that the AuDBNP penetrated the KCl droplet always at the same angle, crucial for consistency between different experiments, the pipette was held on the coverslip with a custom-made PTFE holder.



Fig. 3.4 Customised coverslip set-up: the custom-made PTFE holder is secured on a glass coverslip, containing a droplet of KCl, within a glue boundary, hosting the RE. The tip penetrates the KCl droplet, and the open barrel, where the WE is placed, is filled with the solution of DNA and KCl.

3.2.3 Faraday Cage

To minimise noise and interference from the surrounding environment, all electrical measurements were performed inside a Faraday Cage. In particular, the

experiments requiring laser illumination were performed in the customised Faraday Cage reported in Figure 3.5a. The cage was equipped with a front sliding door, and presented a rectangular opening at the bottom for sample holding and optical access, and a circular opening at the top for wires. A portable eONE amplifier (Elements srl) was fixed inside the cage, together with a LED light.

The coverslip assembly was inserted over the objectives in the rectangular opening of the cage, and the electrodes were connected to the amplifier. The cage was grounded and mounted on a motorised stage and, in order to maximise insulation and stability, the bottom of the cage was covered in Parafilm, leaving the bottom opening clear. The stage was controlled with a joystick that allowed movement in the x and y directions. To further minimise the noise, all measurements were conducted with the room lights and LED switched off.

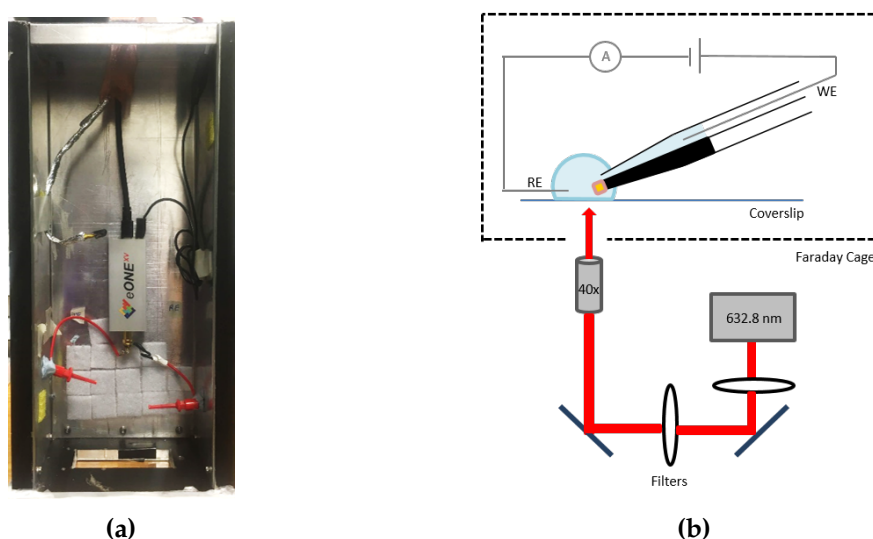


Fig. 3.5 Customised electrical detection set-up integrated with laser optics to enable temperature modulations: (a) The customised Faraday cage used for measurements, containing the eONE portable amplifier, LED light, and WE and RE connectors. The bottom opening served as optical access. The cage was mounted on a motorised stage, and all the measurements were performed with the cage closed and the lights switched off. (b) Schematic of the coverslip set-up and integration of laser optics: the laser beam power can be tuned by two sets of attenuating filters, before being directed to the pipette through the objective.

3.2.4 Integration of Laser Optics

To induce local heating at the tip of the AuDBNP, a He/Ne laser having a wavelength $\lambda = 632.8$ nm was passed through a series of optical density filters before being directed to the pipette through a x40 objective (air immersion, Olympus LUCPLANFLN, 4.00 mm WD, 0.60 NA, 1287 nm spot size). The filters along the

laser path allowed to tune the power of the incoming beam between 0 mW and 17 mW. Using the DinoCapture 2.0 software (Dino-Lite, UK), the position of the laser spot was marked on the computer screen, then the x40 objective was used to focus the tip of the pipette and the stage was moved to align it with the laser spot. Figure 3.5b presents a simplified schematic of the coverslip set-up and laser path (not to scale).

3.3 IV and Conductivity Measurements

IV characterisation measurements of the pipettes were conducted either on AxoPatch 200B patch-clamp amplifier (Molecular Devices), using ramping voltammetry, or eONE amplifier by staircase voltammetry. In the first case, reported in Figure 3.6a, the voltage was ramped from 0 mV to twenty equally spaced potentials between -500 mV and +500 mV, for a total of 107 ms. The voltage was then held at that value for 250 ms, and finally ramped back to 0 mV. The corresponding current was recorded. The resulting IV curves were obtained using ClampFit (Molecular Devices, USA). For the staircase voltammetry, shown in Figure 3.6b, the applied voltage was ramped from -500 mV to +500 mV at 100 mV steps, with every step being held for 4 s. Every cycle was repeated 2 times and the corresponding current was recorded. The data was further processed to obtain the IV curve.

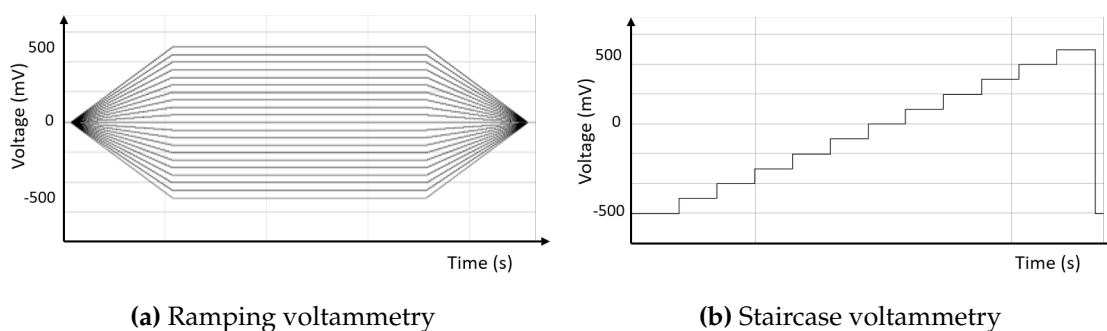


Fig. 3.6 Protocols used for IV measurements

3.4 DNA Translocations and Data Analysis

3.4.1 DNA Translocations

When performing DNA translocation experiments, the open barrel of the AuDBNP was filled with the 400 pM 10 kbp DNA solution and the pipette tip was inserted

in the 100 mM KCl solution, as shown in Figure 3.7. The Ag/AgCl working electrode was inserted in the pipette, while the reference Ag/AgCl one was placed in the external bath. DNA translocations were then conducted from the inside to the outside of the pipette. The ionic current was measured either using the AxoPatch 200B amplifier or the eONE amplifier, both set in voltage-clamp mode, and the data recorded, using either pClamp 10.2 software or Elements Data Reader software, was filtered at 10 kHz.

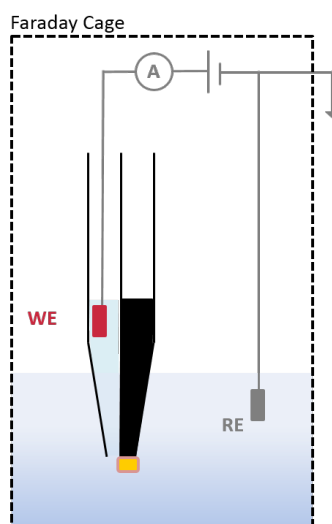


Fig. 3.7 Basic schematic of a DNA translocation experiment on a AuDBNP: the open barrel with the WE is filled with the solution of KCl and DNA, while the RE is dipped into a KCl bath. The set-up is placed in a grounded Faraday cage. A potential is applied and the resulting current is recorded.

3.4.2 Data Analysis

The analysis of the recorded current traces was performed using a custom-written code on MATLAB (MathWorks). The baseline current was calculated for every 5 data points, and a threshold was set as the standard deviation (6-12 pA) from the baseline current. DNA translocation events were determined as the peaks lying above the threshold. Dwell times were computed considering a FWHM of 5, and blockade/peak current was calculated as the current peak maximum after baseline subtraction.

Chapter 4

Results and Discussion

4.1 Pipette Fabrication

The first step to achieve control over the temperature and the local environment of the nanopore, and thus manipulating DNA translocations, was to fabricate a reliable and robust platform where to carry out the experiments. As explained in the Introduction, the device proposed consists of a modified dual-barrel nanopipette, in which one of the barrels is filled with amorphous carbon, and gold, which acts as heating element upon laser exposure, is electrodeposited at the tip.

The first two stages of fabrication, reported in Chapter 3, and whose reproducibility and reliability has been proven by a various studies [68, 69, 86, 87], include the laser pulling of the quartz capillaries, to produce the dual-barrel nanopipettes, and the pyrolytic deposition of amorphous carbon in one of the barrels.

Even if characterising nanopores with a diameter smaller than 50 nm can be challenging [68, 87], the fabricated tips were successfully characterised before and after carbon deposition, using optical microscopy and SEM. Figure 4.1a reports SEM images of an unmodified dual-barrel nanopipette, displaying a clear boundary between the two barrels, which indicates that it is possible to selectively deposit carbon in one of the barrels only. A bright-field microscopy image of the pipette after pyrolytic carbon deposition is shown Figure 4.1b, where the distinction between the unmodified clear barrel and the one filled with amorphous carbon is clearly visible.



Fig. 4.1 Characterisation of the fabricated dual-barrel nanopipettes, before and after pyrolytic carbon deposition: (a) SEM image highlighting the two pores at the tip of a plain dual-barrel nanopipette; (b) Bright-field optical micrograph of the pipette after carbon deposition, demonstrating the successful deposition within one barrel (shown in black), while the other remains unmodified.

4.1.1 Gold Electrodeposition

After the successful fabrication of the pipettes, and the deposition of carbon in one of the barrels, the following fabrication step comprises the electrodeposition of gold at the tip of the carbon barrel. Upon laser exposure, the metallic structure will act as a local heater, through the excitation of surface plasmons. The choice of using gold as plasmonic material resides in its high thermal conductivity and chemical stability [65, 70].

In the present work, the deposition of gold was achieved using a method previously proposed by members and collaborators of the Edel Group [59, 60, 88] and optimised for dual-barrel nanopipettes by Xue [89]. The fabrication was carried out in a biopotentiostat and the schematic of the setup is reported in Figure 3.3. The potential of the two working electrodes was controlled independently, the one inserted in the carbon-barrel (WE_1) induced the gold deposition, while the one inserted in the open barrel (WE_2) monitored the real-time ionic current.

As explained in Chapter 3, the deposition of gold was obtained using ECF64 plating solution, by applying a constant potential of -0.73 V to WE_1 , which induced the two step reduction process detailed in Eq. 3.1 and 3.2. The potential of -0.1 V applied to WE_2 induced an ionic current $i_{feedback}$, which was used to monitor the dimensions of the pore at the tip of the open-barrel. Figure 4.2 reports example current traces associated to deposition and feedback, and the IV characteristic before and after deposition.

The deposition current, reported in Figure 4.2a(i), displays an initial gradual increase (in absolute value), followed by a steeper increase with time, which indicates that the deposition is occurring faster. This is consistent with what reported by [89]: the deposition of gold on the carbon tip occurs via nucleation

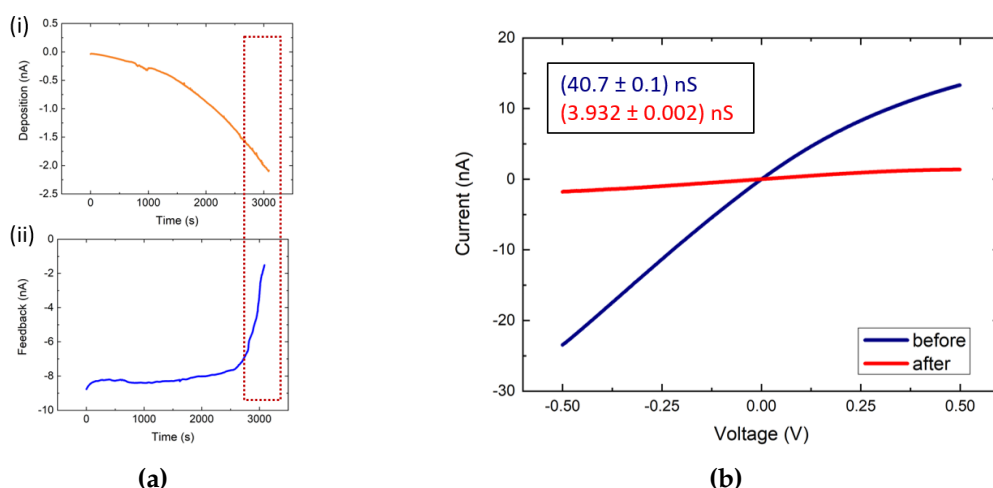


Fig. 4.2 Current traces associated to the gold deposition process: (a) Example of I-t traces related to (i) the deposition and (ii) the feedback. The highlighted area corresponds to the fast pore-shrinking regime. (b) IV characteristic of the pipette before (blue) and after (red) the gold deposition. The conductance was calculated as a linear fit between -0.1 V and 0.1 V .

first (a slower process associated to a low current), and, after this stage, the electrodeposition accelerates with time. The feedback current, displayed in Figure 4.2a(ii) is associated to the pore conductance and, hence, the pore dimensions. Up to 2500s, the current remains almost constant at -8 nA , after which an abrupt decrease (in absolute value) is observed, highlighted in 4.2a(ii). This phenomenon is associated to a rapid pore-shrinking due to the growth of electrodeposited gold over the open-barrel. By closely monitoring the feedback current, it is possible to control the pore conductance, by stopping the deposition process when $i_{feedback}$ reaches a certain value. In the present work, to ensure consistency between the fabricated pipettes, the gold electrodeposition was always halted when $i_{feedback} = -1.5 \text{ nA}$.

The variation in pore conductance can be further investigated by measuring the IV characteristic of the pipette before and after the deposition, as reported in Figure 4.2b, which confirms the occurrence pore shrinking. The figure also reveals that, both before and after deposition, the IV deviates from linearity. More in detail, under relatively large negative voltages, the magnitude of the ionic current is higher than under the corresponding positive voltage. In this case, the phenomenon is called negative rectification, and it is associated to the surface charge present on the glass walls of the pipette. In alkaline solutions, like $(\text{NH}_4)_2\text{SO}_3$ and KCl (the ones used during gold electrodeposition and DNA translocation experiments, respectively), the dissociation of surface hydroxyl groups on the quartz glass causes the walls of the pipette to be negatively charged

[29]. In turn, this gives rise to the formation of a diffusive double layer (DDL), where cations (NH_4^+ or K^+) are accumulated, to compensate for the negative surface charge, and anions (SO_3^- or Cl^-) are depleted. At the scale of the present experiments, the extension of the DDL (~ 1 nm [90]) is comparable to the pore diameter, which means that when flowing in and out of the tip, ions have to pass through the DDL. As a consequence, the movement of cations is favoured over the movement of anions, and this is mirrored in the asymmetry of the IV curve.

To avoid including the effect of negative rectification, the conductance of the pipette can be retrieved by performing a linear fitting on the IV curve between -0.1 V and 0.1 V, where the deviation from linearity is less pronounced. Before gold electrodeposition, the calculated conductance was 40.7 ± 0.1 nS, after deposition it was reduced to 3.932 ± 0.002 nS.

This fabrication step showed a good reproducibility, almost all the pipettes produced displayed the same deposition dynamics, as highlighted in Figure 4.3, which reports sample deposition I-t and IV traces of 4 different tips. Since the pore size, conductance and the size of the deposited carbon area can vary significantly between different pipettes, the time required to reach the fast pore-shrinking regime showed considerable fluctuations, ranging between 1000s to 3000s. However, by stopping the deposition always at the same level of $i_{feedback}$, in this case -1.5 nA, it was possible to tune the pore conductance and achieve consistency among the fabricated pores.

4.1.2 Characterization of Modified Pipette

Optical Characterisation

The fabricated AuDBNPs were further characterised via optical microscopy and SEM imaging, as shown in Figure 4.4. The first method benefits of a simple sample preparation, which enables to easily visualise the results of the gold electrodeposition. Figures 4.4a and 4.4b report two images of the tip obtained using bright-field microscopy, using a top light and a bottom light, respectively. The formation of a circular gold bulb at the tip of the pipette is clearly visible. This is confirmed by Figure 4.4c, obtained via dark-field microscopy, where the light scattered by the sample produces the optical contrast.

Figures 4.4d-f, obtained through SEM microscopy, provide additional information about the deposition pattern, with higher sensitivity and resolution than optical microscopy. The deposited gold bulb, which has micrometer dimensions, displays a rough and irregular pattern, which, upon laser exposure, will enhance

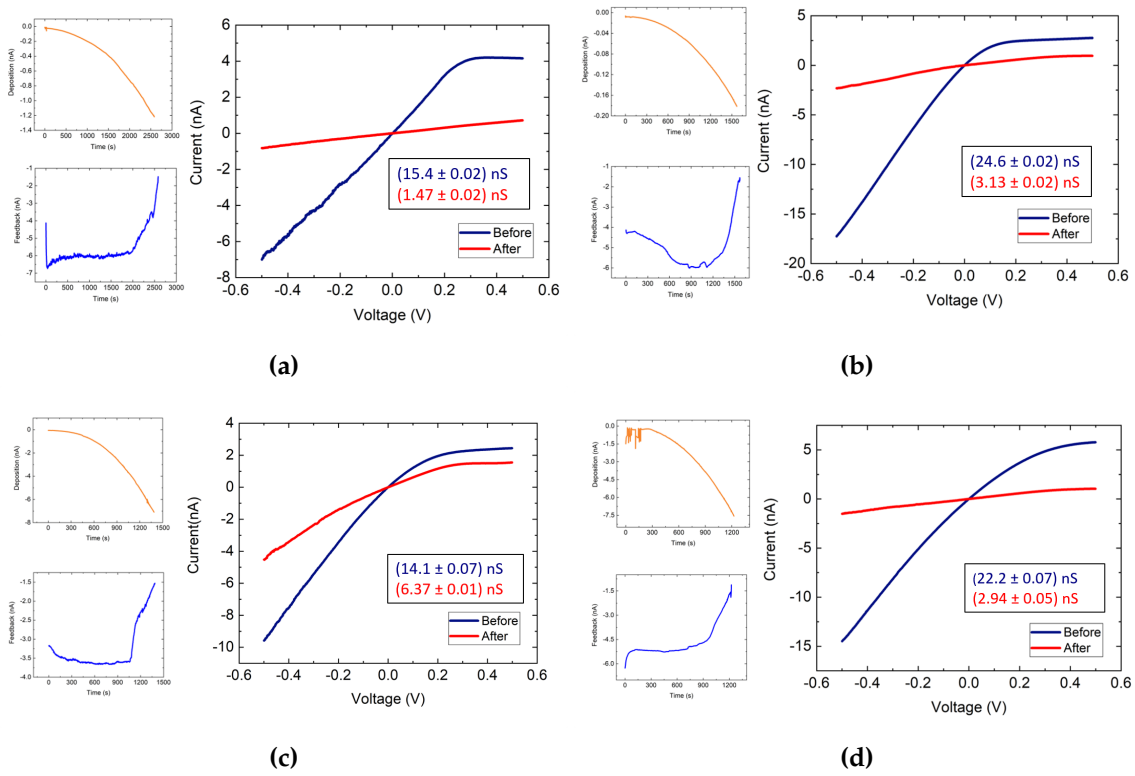


Fig. 4.3 Examples of current traces associated to the gold deposition process to demonstrate the reproducibility of the process and the control over the final conductance of the pipette.

the excitation of surface plasmons. Moreover, the side images of the tip (Figures 4.4d and 4.4f), show that, when growing, the gold completely surrounds the tip, ensuring a uniform heating of the local environment when exposed to laser radiation. Although from Figure 4.4e the pore is not visualised, the IV curves after deposition ensure that the open-barrel pore is still present and not blocked.

Pore Dimensions

Using the conductance values extracted from the linear fitting of the IV characteristic between -100 mV and 100 mV, and assuming that the pore has a cylindrical shape, it is possible to obtain a rough estimate of the inner diameter of the pore of the open barrel, using the following equation [47]:

$$d = \frac{4Gl}{\pi\delta d_b} \quad (4.1)$$

In Eq 4.1, G is the conductance, l is the the length of the conical-shaped part of the pipette (1.5 mm), δ is the electrolytic conductivity of 100 mM KCl (1.285 S/m [91]), and d_b is is the inner diameter of the capillary before convergence

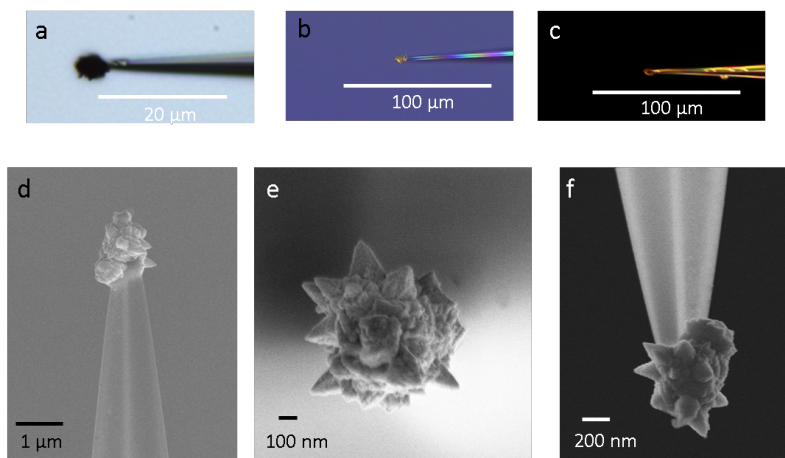


Fig. 4.4 Characterisation of the fabricated pipettes after Au deposition: (a-b) Bright field images of the tip of the pipette, top light and bottom light respectively. (c) Dark field image of the tip. (d-f) SEM images of the tip, (d) and (f) display lateral views, (e) is zoom-in from the top of the tip.

(0.5 mm). The fabricated AuDBNPs exhibit a typical conductance of 8.7 ± 0.5 nS, calculated from an average of 10 nanopipettes, which results in an inner diameter of roughly 25 ± 1 nm, which is in good agreement with other studies on nanopipettes [47, 56, 62, 92, 93]

4.2 Local Temperature Modulation

Having established a reliable and reproducible fabrication process, which yields a robust device, adequate for the excitation of surface plasmons, the following step was to establish an experimental apparatus which integrated the more conventional electrical detection with laser optics, while maintaining a minimal level of noise.

4.2.1 Integrating Laser Heating with Nanopore

Faraday Cage and Laser Alignment

As explained in Chapter 3, the experiments were conducted inside the custom-made Faraday Cage depicted in Figure 3.5a. The rectangular opening at the bottom enabled optical access, while the circular opening at the top was used to insert the wires. The inside of the cage was equipped with the eONE portable amplifier with connectors, used both to apply potential on the pipette and to record the resulting current, and with a LED light. The cage was grounded, to minimise noise

interference, and, to improve insulation and stability, the bottom, except for the rectangular opening, was covered in Parafilm. The cage was mounted on a motorised stage, controlled with a joystick, which enabled accurate alignment of the tip of the pipette with the laser spot. Usually, to eliminate radiative pick-up noise, a double-nested Faraday cage is used [94], however, due to set-up limitations, in the present work, the microscope, camera, laser source, and computer were not encased. To compensate for this, all the experiments were carried out switching the lights off, which significantly reduced the noise levels to 10-20 pA (Standard deviation, STD, of the current baseline), comparable to typical literature values [76, 82].

The pipette was inserted in the Faraday Cage using the coverslip assembly reported in Figure 3.4. The customised PTFE holder ensured that the tilt-angle of the pipette and the incidence angle of the laser radiation remained almost constant throughout different experiments. All the DNA translocation studies were performed by applying a negative potential to the WE, which induced the translocations to occur from the inside of the pipette to the outside. The laser radiation was directed to the tip as reported in the schematic of Figure 3.5b, and focused via the 40x objective of the microscope. The two sets of filter-wheels present on the laser path allowed to tune the incident power from 0 to 17 mW, and to completely block the radiation when needed. The set-up used was equipped with two laser sources, one having $\lambda = 632.8$ nm (red light) and one with $\lambda = 532$ nm (green light).

To ensure that the effects of the laser illumination were maximised, a crucial step to be performed was the accurate alignment of the nanopipette's tip, and gold bulb, with the laser spot. To do so, firstly the laser spot was focused through the 40x objective, and its position mapped out on the computer screen. Then, the incoming laser light was temporarily blocked and the pipette tip was focused. Finally, the tip and the gold bulb were aligned with the laser spot position, by moving the stage along the x and y directions. A more precise alignment was achieved by using the ionic current enhancement induced by laser illumination. The tip's position at which the current enhancement was maximised was the one used for experiments. To compensate for any possible pipette's drift over time, realignment was periodically performed during experiments.

Laser Wavelength

As mentioned above, the experimental set-up was equipped with two different laser sources, $\lambda = 632.8$ nm and $\lambda = 532$ nm. To choose the most appropriate one

for the present investigation, the noise introduced by laser illumination of the AuDBNPs was investigated and compared between the two wavelengths.

Figure 4.5 reports the current baseline STD and the Power Spectrum Density (PSD), for different voltages and different laser powers. By comparing Figures 4.5a(i) and 4.5b(i), it is clear that the 532 nm laser introduces high noise components, up to 210 pA, for all the voltages and powers considered, while the noise associated to the 632.8 nm laser remains below 80 pA. Considering that, for Au-DBNPs, the mean amplitude of a translocation signal is roughly 150 pA [89], the results on the baseline STD mean that the noise introduced by exposure to the 532 nm laser would mask the DNA translocation signals, making the data analysis troublesome. Moreover, considering the PSDs associated to the two lasers, Figures 4.5a(ii) and 4.5b(ii), exposure to the red laser introduces negligible additional noise, compared to the green one, which is consistent with previous findings [70, 80]. Therefore, all the investigations on DNA translocations were performed using the 632.8 nm laser.

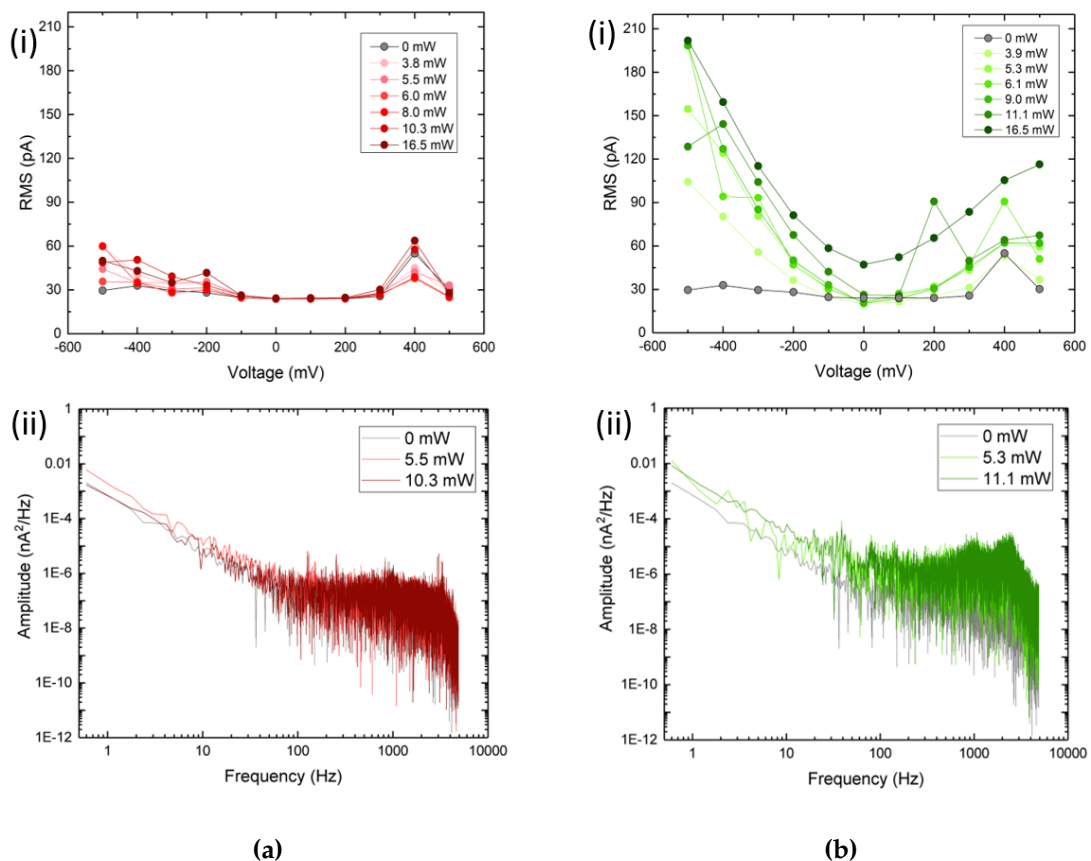


Fig. 4.5 Comparison of the noise levels associated to laser irradiation, for two different laser wavelengths: (a)(i) -(b)(i) STD of the baseline current as a function of voltage and laser power; (a)(ii)-(b)(ii) PSD under three different laser powers for $\lambda=632.8$ nm and $\lambda=533$ nm, respectively.

The differences in the noise components derive from the diverse mechanisms of heating induced by the two lasers. The 532 nm one is efficiently absorbed through interband transitions in gold. This results in a less-controlled heating of the bulk area surrounding the nanopore, and in an increase in electrical noise. In contrast, the 632.8 nm laser excites surface plasmons on the gold, which then decay through non-radiative absorption, locally heating the gold and nanopore [70, 80, 81]. Even if lower, the heating provided by the 632.8 nm laser is sufficient and local, and the noise induced is low and almost constant for the different laser powers, making it suitable for experiments with AuDBNPs.

4.2.2 IV and Conductance Modulation

To quantify the extent of laser-induced heating on the nanopores, the IV characteristics of Carbon-deposited dual-barrel pipettes (C-DBNP) and of AuDBNPs were recorded under illumination. The results can be seen in Figures 4.6a and 4.6b. In the case of a C-DBNP, the changes due to laser exposure are minimal, while for a AuDBNP, the ionic current modulation is significant, showing a more than 100% increase at full power (16 mW). The differences between the two situations are further highlighted by Figure 4.6c, which reports the relative current enhancement I/I_0 at -500 mV for increasing laser powers. The substantial modulation exhibited by the AuDBNP confirms the function of gold as an adequate local heater.

The increase in ionic current can be explained considering that heating reduces the viscosity of the solution, thus increasing the mobility of the K^+ and Cl^- ions, and the buffer conductivity [81, 84]. The differences between the C-DBNPs and the AuDBNPs are related to the fact that gold absorbs 632.8 nm radiation much more efficiently than quartz, therefore the resulting heating is more pronounced. It must be pointed out that, due to inherent differences among pipettes in terms of geometries and gold bulb size, the laser-induced enhancement is not exactly the same, but the overall effect remains unchanged.

Another important consideration to be done is related to the stability of the ionic current under laser illumination. The traces reported in Figure 4.6d demonstrate that the baseline current remains stable when increasing the laser power, which is crucial for performing successful DNA translocation studies. In addition to this, the trace reported in Figure 4.7, which displays a recording of the ionic current under a bias of -400 mV and pulsed laser illumination, highlights two other key-factors of the laser-induced enhancement. The current changes are *instantaneous* and *reversible*. When the laser is switched on, the current reaches the higher value in a time-frame of the order of milliseconds, as emphasised in Figure

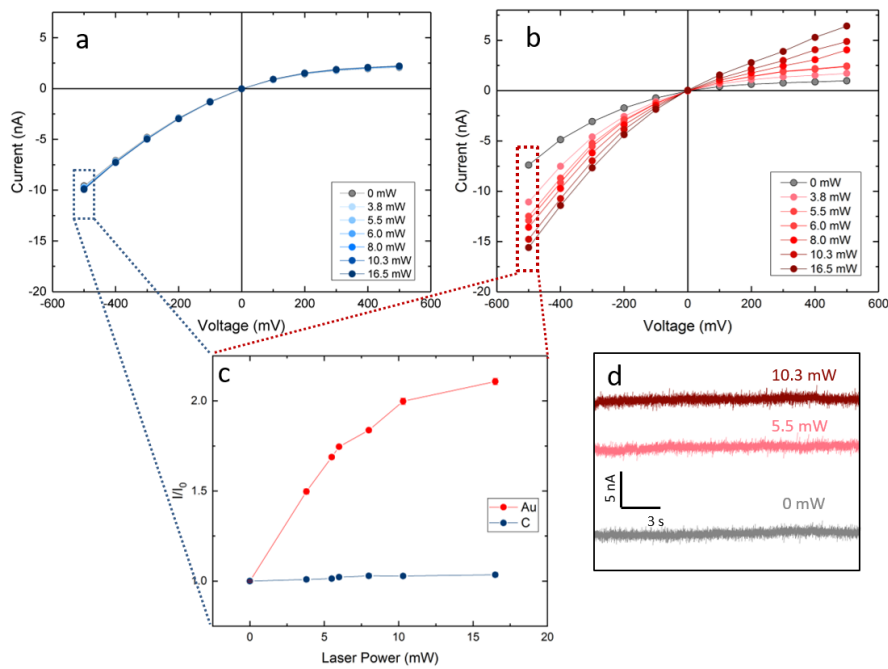


Fig. 4.6 Effects of the laser induced-local heating on the ionic current: (a-b) IV characteristic under 633 nm laser, for different laser powers, for a C-deposited pipette and a AuDBNP, respectively. (c) Relative current enhancement as a function of laser power, for the two pipettes considered, at -500 mV. (d) Comparison of the baseline current stability for the AuDBNP for different laser powers, at -500 mV.

4.7b, and, when the laser is switched off, the current goes back to its original value, with a similar time scale. The almost-instantaneous and reversible control over the ionic current is essential for achieving rapid manipulation of molecular transport during DNA translocations.

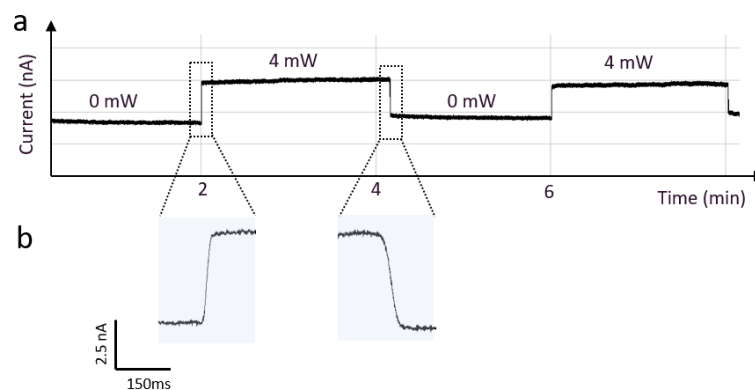


Fig. 4.7 Instantaneous and reversible changes induced by laser illumination on the AuDBNP: (a) I-t trace recorded at -400 mV with pulsed laser illumination, each segment has a duration of 2 minutes. (b) Highlight of the current enhancement induced by laser exposure and the reversible current reduction once the laser is turned off.

4.2.3 Temperature Conversion

In order to use the pipette as a nanoscale temperature probe, the ionic current modulations have to be directly related to temperature changes. At a given bias voltage, the ionic current I of a pore is linearly dependent on the ionic bulk conductivity σ_{bulk} [82]:

$$I(T) = A\sigma_{bulk}(T) = A(a + bT) \quad (4.2)$$

where A is linked to pore geometry, and a and b are two experimental constants related to bulk conductivity. When the temperature changes from T_1 to T_2 , the resulting relative current change $\Delta I/I$ can be computed as:

$$\frac{\Delta I}{I} = \frac{a + bT_2 - a - bT_1}{a + bT_1} = \frac{b(T_2 - T_1)}{a + bT_1} = \frac{b\Delta T}{a + bT_1} \quad (4.3)$$

By rearranging Eq. 4.3, the temperature change can be estimated from the relative current change induced by laser heating as [80, 82]:

$$\Delta T = \left(\frac{a}{b} + T_0 \right) \times \frac{\Delta I}{I} \quad (4.4)$$

where T_0 is the starting temperature, in this case T_0 is the room temperature, 22.5 °C.

The experimental constants a and b were retrieved by measuring the conductivity, in terms of concentration, of a bulk solution of 100 mM KCl in TE buffer, as a function of temperature. The results are shown in Figure 4.8 and, as expected, conductivity is linearly dependent on temperature. A linear fitting was performed to extract the values of a , slope, and b , intercept, which are found to be 3.0 ± 0.2 and 0.16 ± 0.01

By assuming that nanoscale conductivity σ_{nano} is linear with temperature like bulk conductivity σ_{bulk} , $\sigma_{nano} = A\sigma_{bulk} = A(a + bT)$ [82], Eq. 4.4 can be used to quantify the temperature changes that occur in the local environment of the AuDBNP (and C-DBNP) upon laser exposure, for the different incoming powers. The results of the conversion are reported in Figure 4.9a, which confirms the efficiency of the gold-modified device to generate significant local heating. Figure 4.9b displays the conductance of the AuDBNP (extracted from the IV characteristics) as a function of temperature, which agrees with the assumption of the linearity of nanoscale conductivity. A deviation from linear behaviour would imply the presence of local thermal gradients and thermophoretic effects

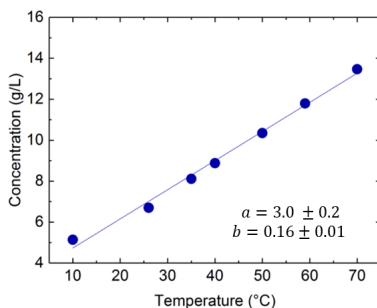


Fig. 4.8 Linear fitting of the conductivity of bulk KCl: the conductivity of 100 mM KCl in TE buffer was measured, in terms of concentration, as a function of temperature. The experimental constants a and b are the slope and intercept of the fitting line, respectively. $R\text{-Sq} = 0.99$, for the linear fitting.

around the pore, as highlighted in previous studies [81]. Owing to the validation of conductance linearity, in the present study, Eq 4.4 was used to quantify all the temperature changes associated to laser exposure.

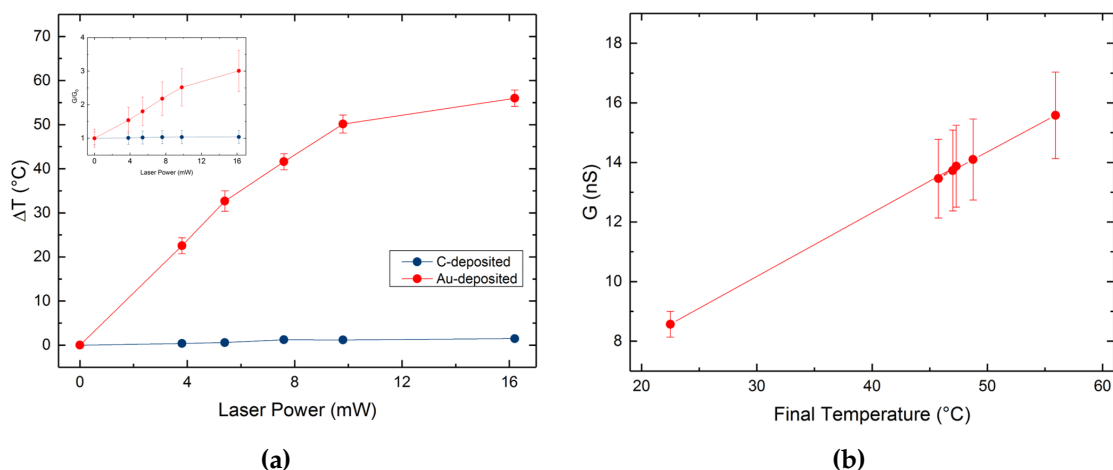


Fig. 4.9 Temperature changes associated to laser exposure and pipette's conductance as a function of temperature: (a) Comparison of the induced temperature change as a function of laser power, for C-DBNP and AuDBNP. The errors are calculated from the STDs of the baseline current. The inset shows the conductance enhancement, G/G_0 , where the conductance is extracted from the slope of the IV curves between -100 mV and 100 mV. (b) AuDBNP conductance as a function of temperature, which is confirmed to be linear. $R\text{-Sq} = 0.99$, for the linear fitting.

4.2.4 Stability of the System

Before starting the actual experiments on DNA translocations, it was essential to probe the stability and the reliability of the device under the high temperatures induced by laser irradiation. Prolonged exposure could lead to various, sometimes irreversible, consequences: partial gold detachment, expansion of the glass of the

pipette, generating a larger pore, and evaporation of KCl, resulting in a more concentrated electrolyte [84].

To investigate the extent of the effects of laser heating, three different tests were carried out. Firstly, the ionic current of a pipette exposed to 8.3 mW of laser power, under a bias of -400 mV, was recorded for an hour. The resulting trace is reported in Figure 4.10a: for the first 20 minutes the current remained fairly stable, suggesting that the laser-induced heating hadn't caused any major changes in the pipette's environment. After 20 minutes, the current started to increase slightly and to manifest some minor instabilities. Then, above 40 minutes of constant laser exposure, the fluctuations of the current became more pronounced, hinting at significant changes of the pipette. In order to ensure the reliability of the DNA translocations studies, all the experiments were carried out in the "safe-zone", within a time-frame of 20-30 minutes.

The second stability test consisted in comparing the IV characteristic of the pipette at three different stages: before exposure, after 6 minutes of exposure, and after refilling the barrel and the external reservoir with fresh KCl, as shown in Figure 4.10b. As it can be noted, even a brief exposure to laser causes some minor changes in the IV, but, after adding fresh electrolyte, they are almost-completely restored, suggesting that KCl evaporation might be the reason behind the discrepancy.

Finally, to verify that the changes in IV were due to laser-heating and not to gold detachment, electrochemistry measurements were performed using the redox probe $\text{Ru}(\text{NH}_3)_6\text{Cl}_3$ (Aldrich). The AuDBNP was inserted in a solution containing 1mM of $\text{Ru}(\text{NH}_3)_6\text{Cl}_3$ in 100 mM KCl and potential was applied on the carbon-filled barrel via a Cu electrode. By negatively polarising the gold at the tip, using linear sweep voltammetry from 0 V to -0.45 V, the redox probe is reduced. The reaction occurring on the gold surface is the following:



As the negative voltage applied increases, the reaction is limited by the amount of Ru that can diffuse on the Au surface, and after -0.35 V, the current remains roughly constant. Assuming a spheric shape for the gold bulb at the tip, from the value of the diffusion limited current it is possible to estimate the radius of the gold as reported below [89, 95, 96]:

$$r = \frac{I_{\text{steadystate}}}{4.64nFCD} \quad (4.6)$$

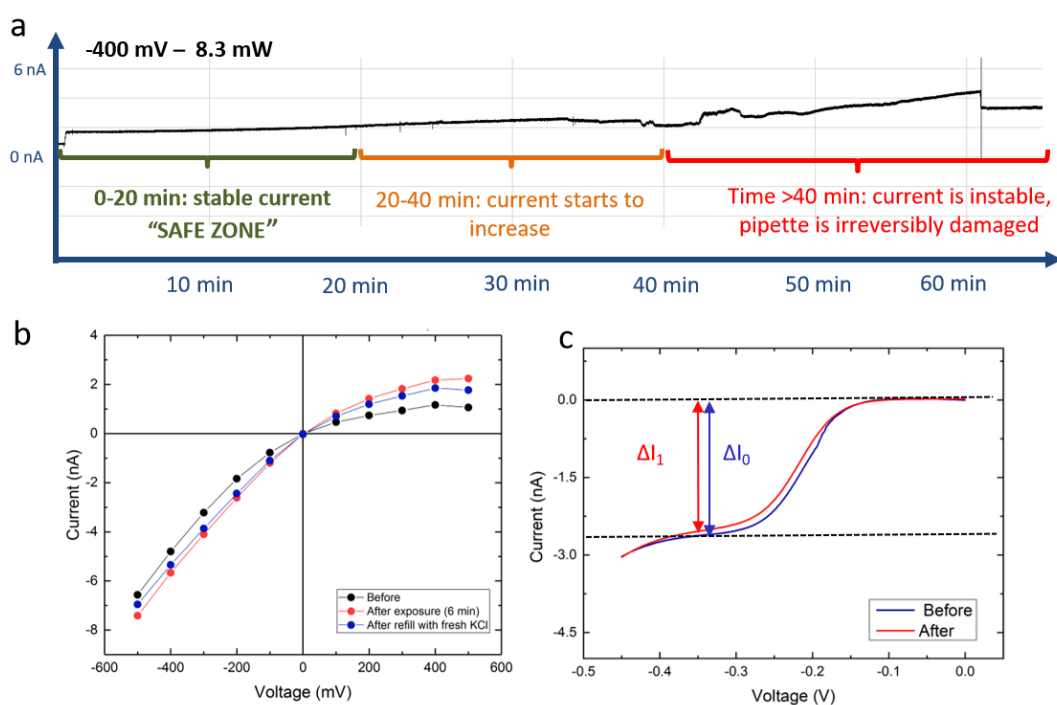


Fig. 4.10 Stability of the system: (a) Current trace recorded for 60 minutes, at -400 mV and under 8.3 mW of laser illumination, showing the effects of prologued laser exposure. (b) IV of the pipettes at different moments during the experiment: before exposure, after 6 minutes of exposure, after refilling the open-barrel and the external bath with fresh KCl. The minimal variations in IV confirm that no significant change has occurred to the pipette. (c) Diffusion limited current on the surface of the deposited Au, which confirms that no gold detachment occurs upon laser exposure.

Where

- $n = 1$, number of electrons exchanged in the reaction;
- $F = 96485$ C/mol, Faraday constant;
- $C = 1$ mM, concentration of $\text{Ru}(\text{NH}_3)_6\text{Cl}_3$;
- $D = 8.4\text{E-}10$ m²/s, diffusion coefficient in 100 mM KCl [96].

The electrochemistry measurement was performed before and after 10 minutes of laser exposure, and the current traces obtained are reported in Figure 4.10c. The ratio between the relative changes in current ($\Delta I = I(0\text{V}) - I_{\text{steadystate}}(-0.35\text{V})$) is equal to the ratio of the areas of the gold bulb.

$$\frac{\Delta I_1}{\Delta I_0} = \frac{A_1}{A_0} = 0.98 \quad (4.7)$$

The corresponding radius are $r_0 = 6.9\mu m$ and $r_1 = 6.8\mu m$, which confirms that controlled laser exposure causes negligible detachment of gold from the tip.

4.3 Controlling Single-Molecule DNA Translocations

After having successfully established a reliable method to tune the temperature in the local environment of the pore, the system was employed to study the effect of temperature modulations on DNA translocation dynamics. All the experiments were performed using 10 kbp DNA (400 pM) in 100 mM KCl in TE buffer (pH 8 at room temperature), with the translocations occurring from the inside to the outside of the pipette.

4.3.1 DNA Translocations through Plain and Gold Pipettes

When DNA translocates through a pore, as mentioned in the introduction, three main parameters that characterise the process can be extracted: dwell time t_d , blockade current I_B , and capture rate R_C . Figure 4.11 reports the results obtained for DNA translocations occurring in a plain dual-barrel pipette, conducted on the AxoPatch set-up, to illustrate the typical behaviour of the three key-parameters with varying bias voltage.

The phosphate groups on the DNA backbone impart the molecule a negative charge, therefore, under a negative bias, the DNA moves from the inside to the outside of the pore. In general, the translocation process is governed by an interplay of diffusion, electrophoretic and electroosmotic forces [3, 29], which determine the type of voltage dependence of t_d , I_B and R_C . Away from the pore, DNA motion is governed by diffusion, and it is non-directional. When the DNA reaches a certain distance r^* , denoted as capture radius, the electrophoretic force induced by the external bias overcomes the random diffusive motion, and the molecule is directed towards the pore. In order to give rise to a successful translocation, the DNA molecule has to overcome an entropic barrier, associated to the conformational changes needed to unravel the DNA to thread through the pore. As the applied voltage increases, the entropic barrier associated to DNA stretching into the pore is reduced [28, 45, 97–99].

The **dwell time**, Figure 4.11b, shows a decreasing trend with increasing bias, which is due to the fact that at higher voltages the electrophoretic force on the translocating molecule rises. This produces higher translocation velocities and, as a consequence, shorter dwell times. The amplitude of the **blockade current** (also

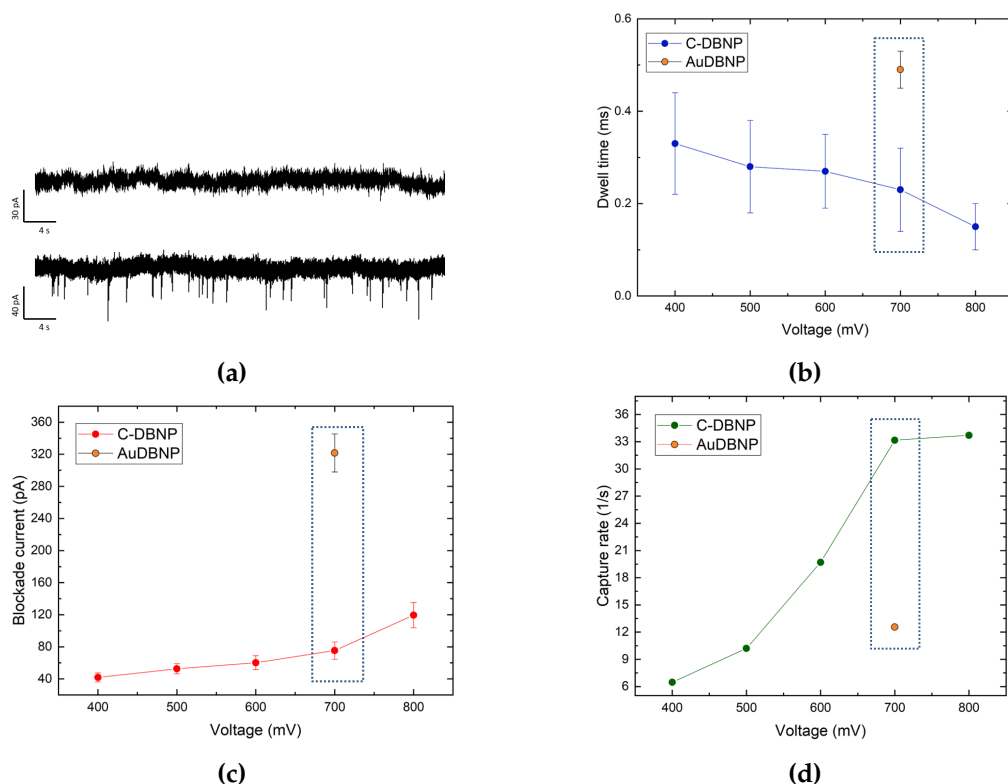


Fig. 4.11 Example of the results obtained from a voltage-dependent translocation study on a plain dual-barrel nanopipette: (a) 4s snapshot of the current at -400 mV before (above) and after (below) adding 10 kbp DNA. The downward spikes are caused by single-DNA molecules threading through the pore. (b) Dwell time (c) Blockade current and (d) Capture rate voltage-dependence. The highlighted region compares the values of t_d , I_B and R_C between plain DBNP and AuDBNP, at -700 mV.

denoted as peak current), depicted in Figure 4.11c, is related to the charge excluded by the DNA passing through the pore and, with increased bias, it increases as well. Finally, concerning the **capture rate**, reported in Figure 4.11d, its increase with voltage is related to the stronger electrophoretic force and, consequently, the larger capture radius. In the present experiment, the capture rate was simply calculated as the total number of events divided by the time-frame considered (here 30 s).

Previous studies by Xue [89] have demonstrated the feasibility of performing DNA translocations on the fabricated AuDBNPs. The study also highlighted a few major differences between plain DBNPs and the gold-modified ones: dwell time and capture rate decrease, probably owing to stronger DNA-nanopore interactions due to the presence of gold, while the mean blockade current increases significantly. These results were confirmed by performing DNA translocations at -700 mV using a AuDBNP, on the AxoPatch set-up. As it can be seen in the highlighted regions of Figure 4.11, the dwell time is increased from 0.23 ± 0.09 ms to 0.49 ± 0.04 ms, the peak current passes from 75.35 ± 10.73 pA to 321.64 ± 23.64 pA, while the capture rate decreases from 33.2 ± 0.2 s⁻¹ to 12.5 ± 0.2 s⁻¹.

4.3.2 Modulating DNA Translocations by Precisely Tuning the Local Temperature

After having established a reliable experimental apparatus and a robust device, adequate for performing DNA studies, the effect of localised heating and the possibility of manipulating the translocation dynamics were investigated.

Control Experiments on Carbon-deposited Pipettes

Firstly, to verify that no other effect apart from the heating produced by the plasmons excited on the gold surface upon laser exposure altered the translocation dynamics, a control experiment with a C-DBNP was performed. The open barrel of the fabricated C-DBNP was filled with 10 kbp DNA (400 pM) in 100 mM KCl in TE buffer, and the pipette was mounted on the coverslip. The assembly was then placed inside the Faraday cage, and the pipette tip was aligned with the 632.8 nm laser spot. The current was recorded at -400 mV, and the 632.8 nm laser powers were increased every 2 minutes. The results reported in Figure 4.12 confirm that exposing the non-plasmonic pipette to laser induces negligible heating and, therefore, negligible effects on the translocation dynamics. The baseline and peak current, Figure 4.12a, remain almost unaltered throughout the duration of the experiment, and the capture rate, Figure 4.12b, does not display any meaningful trend. Overall, this result confirms that no laser-induced optical force acts on the system, as previous studies have reported [84], but solely the localised temperature modulations, arising from the laser-excited plasmons on the gold bulb at the tip of the AuDBNPs, have to be taken into account.

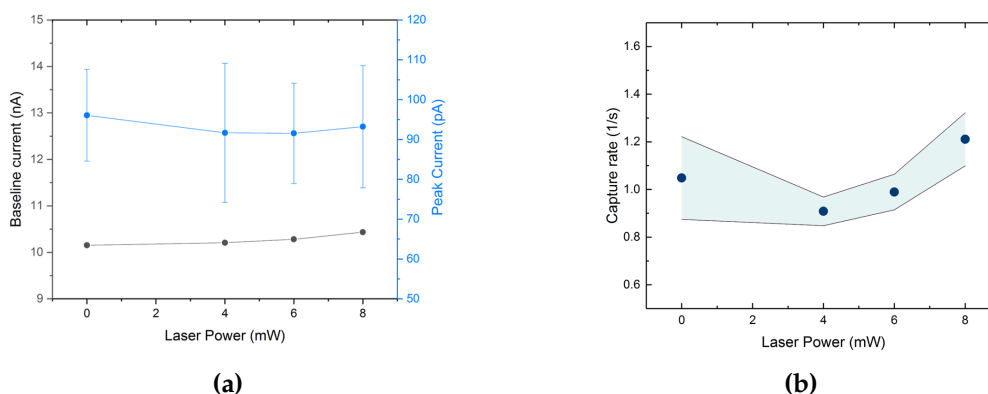


Fig. 4.12 Control experiments on a C-DBNP, confirming the negligible effects of laser exposure on DNA translocations. The experiments were conducted at -400 mV, under 632.8 nm laser exposure. (a) Minimal changes in baseline current and peak current (b) Negligible effects on capture rate, the area highlighted in light blue is determined by the error bars.

Experiments on Gold-modified Pipettes

The fabricated AuDBNPs were filled with 10 kbp DNA (400 pM) in 100 mM KCl in TE buffer, inserted in the Faraday cage on the coverslip assembly, and aligned with the 632.8 nm laser spot. In order to fully characterise the reproducibility and reversibility of the impact of local temperature modulation, two strategies were followed to carry out the experiments, illustrated in Figure 4.13. The time scale of the experiments was chosen in order to obtain a sufficient number of events to perform statistical analysis, while remaining within the previously-defined "safe-zone", Figure 4.10a.

- **Strategy 1 - Sweep of the laser powers:** the current signal was recorded at a constant bias, gradually increasing the power of the incoming laser (positive sweep), followed by the corresponding decrease down to no laser (negative-sweep), Figure 4.13a. Time scale of the experiment ~ 30 min. (Since the pipette is exposed to laser powers lower than the one used in the stability experiment, a time scale 30 min was still considered to be inside the safe-zone).
- **Strategy 2 - Pulsed laser exposure:** the current signal was recorded again at a constant bias, alternating the exposure between no laser and a fixed power, Figure 4.13b. Time scale of the experiment ~ 15 min.

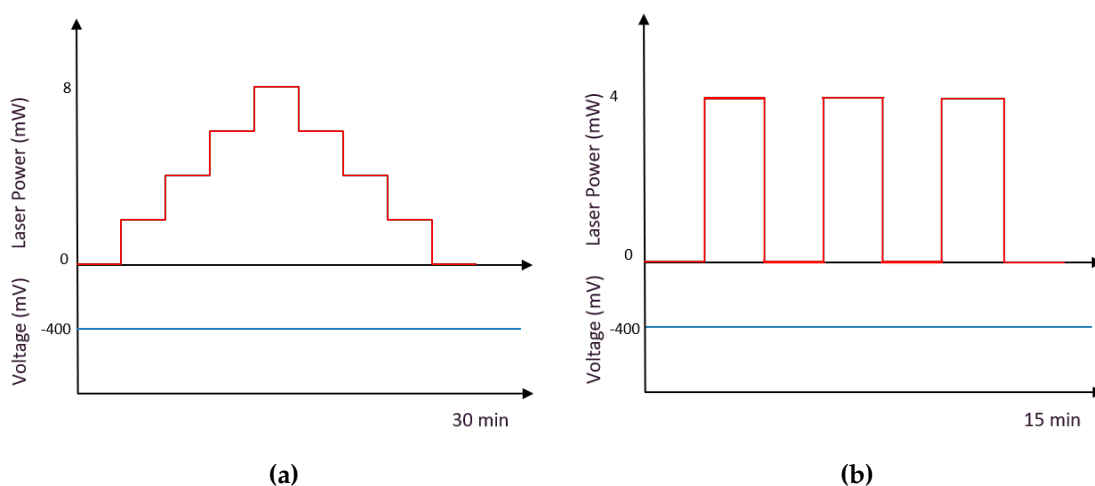


Fig. 4.13 Schematic of the two strategies used to investigate the effects of localised temperature modulation on the DNA translocations: (a) Strategy 1 - Sweep of the laser powers at set time intervals and fixed bias. (b) Strategy 2 - Pulsed laser exposure, at fixed bias and laser power.

Strategy 1 - Sweep of the Laser Powers

To perform experiments following Strategy 1, the ionic current trace flowing through an AuDBNP, was recorded under a bias of -400 mV, while the laser powers were progressively increased, up to 8.3 mW, and then decreased down to 0 mW. Each of the laser powers chosen (0 mW - 2.3 mW - 4.4 mW - 8.3 mW) was maintained for 4 minutes and, as mentioned before, the time scale of the experiments was ~ 30 min. The current was recorded using the eONE amplifier, filtering at 10 kHz. Due to the presence of external noise components, before performing the data analysis, the traces were filtered again, at 2.5 kHz. Even though some details about the translocation peaks were lost, the significant additional filtering was necessary to remove parasite noise that would have otherwise hindered the analysis, making the results unreliable. Regarding the current baseline, the previous analysis had shown that laser exposure didn't cause any major instability, however, introducing DNA in the open barrel induced some minor fluctuations in the current, due to the interaction of DNA molecules with the gold [13, 62, 89].

Figure 4.14 illustrates preliminary results of the translocation studies, both for the positive and negative sweep of laser powers. The panels on the left report the temperatures corresponding to the laser power used. Just by observing the 10s snapshots of the current traces (4.14a(i) and 4.14b(i)) a clear trend can be observed: the number of translocation events increases with temperature, and the enhancement appears to be reversible. The shape of selected individual translocation events (4.14a(ii) and 4.14b(ii)), remained almost unvaried with the temperature ranging between 22.5 °C and 50 °C, always below the melting temperature of dsDNA, and confirms that the peaks observed were indeed translocations. Moreover, the histograms reported in Figures 4.14a(iii) and 4.14b(iii), display an overall shift of the peak amplitude I_B to higher values with increased temperature.

A closer analysis of the translocation parameters, I_B , t_d and R_C , is shown in Figure 4.15. The temperature-induced increase in the signal amplitude is confirmed by Figure 4.15a. However, the relative peak current increase $\Delta I/I$ slightly decreases with increasing temperature, as Figure 4.15b highlights, where $\Delta I/I$ is expressed in terms of relative conductance blockade $\Delta G/G$ (where G is the open pore conductance at the considered laser power and ΔG is the amplitude of the conductance blockade). This result is consistent with other findings in literature [70, 79, 81], and it suggests that the enhancement of blockade levels is simply mirroring the increase in open pore conductance due to the rise in temperature.

The dwell time, does not show any significant variation with temperature, consistently with other studies [81, 99]. It must be noted that the results on the

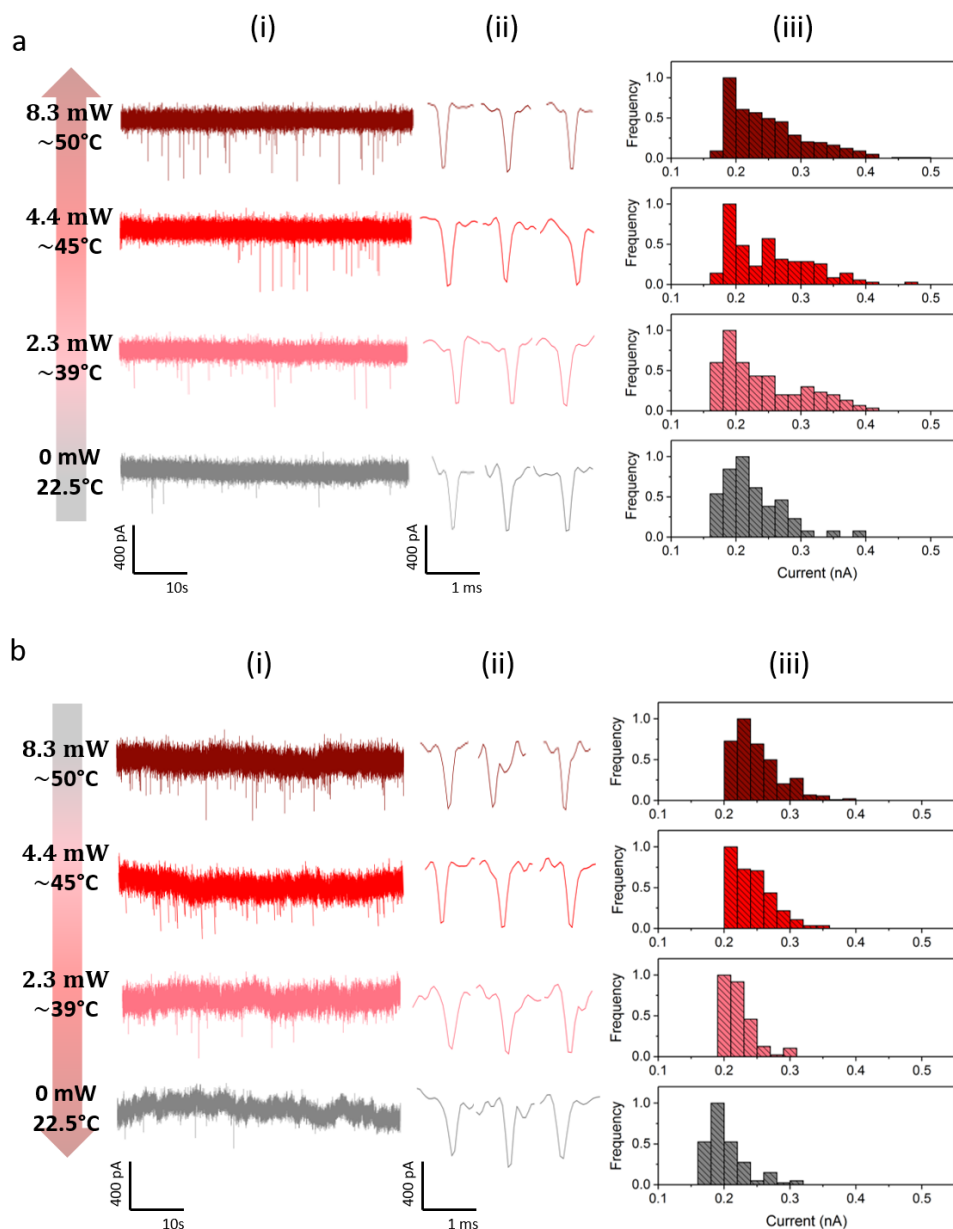


Fig. 4.14 Results illustrating the temperature-induced effects on DNA translocations, using Strategy 1. The experiments were conducted on a AuDBNP at -400 mV, under 632.8 nm laser exposure, for 4 different powers, with the corresponding temperature changes. (a) Displays the results obtained sweeping the laser powers from the lowest to the highest, (b) displays the results for the reversed sweeping (high-to-low). (i) 10s snapshots of the current traces, showing an increasing number of events with increased laser power. (ii) Individual translocation events. (iii) Histograms demonstrating a shift in peak current with increasing laser power.

dwell time are strongly influenced by the set-up used. Due to the presence of the opening at the bottom of the Faraday Cage, and to inherent limitations of the eONE amplifier, the baseline current trace, even if highly stable, was thicker

than usual. More in detail, on the eONE set-up, the current displayed a thickness of ~ 150 pA, while on a standard AxoPatch setup, a typical baseline current is ~ 40 pA thick. Therefore, in the present work, the initial and final part of the translocation ended up being embedded in the baseline, which meant that the variations on the dwell time, if present, could not be picked up during the analysis. Moreover, the bandwidth of a standard AxoPatch setup reaches 100 kHz, while on the eONE it stops at 20 kHz, so details about the translocations are inevitably lost. However, the focus of this work was to investigate whether the local temperature modulations could control the throughput of the system, that is, the capture rate, and, since the translocation peaks were clearly distinguishable from the baseline current, the validity of the results obtained was not hindered by the set-up limitations.

An accurate evaluation of the capture rate, which appears to be enhanced by temperature, was carried out by performing further analysis on the experimental data. As explained before, the process of DNA capture is governed by the interplay of diffusion and voltage-induced forces (electrophoresis and electro-osmosis). At low concentrations, such as the one used in the present work (400 pM), DNA molecules do not interact with each other, and the capture mechanisms can be described as a classic arrival time Poisson process, with no memory effect. Therefore, the normalised probability of arrival time can be modelled with the following equation [28, 75]:

$$P_{\delta t=t}(t) = e^{-t/\tau} \quad (4.8)$$

Where δt is the measured inter-event time (the time between two successive events), and the capture rate $R_C = \tau^{-1}$. The inter-event times were computed as the difference between the starting times of two successive events (which are provided by the custom Matlab code used for analysis) and fitted as mono-exponentials. The capture rate was then calculated as the inverse of the time constant of the exponential decay, and the results are plotted in Figure 4.15c. As expected, the capture rate is significantly enhanced by temperature: between room temperature (22.5 °C- 0 mW) and ~ 50 °C (8.3 mW) it doubles, passing from $1.1 \pm 0.2 \text{ s}^{-1}$ to $2.5 \pm 0.2 \text{ s}^{-1}$ (percentage enhancement ~ 130 %). In addition to this, the increase is reversible. When the local temperature is decreased, by reducing the power of the incoming laser, the capture rate is almost restored to its original value, $1.1 \pm 0.2 \text{ s}^{-1}$ before and $1.4 \pm 0.2 \text{ s}^{-1}$ after. The minor discrepancies between the two values could be due to the fact that, under prolonged exposure, the final local temperature is slightly higher than room temperature. Figure 4.15d reports the exponential fitting of the inter-event times associated to the positive-sweep of

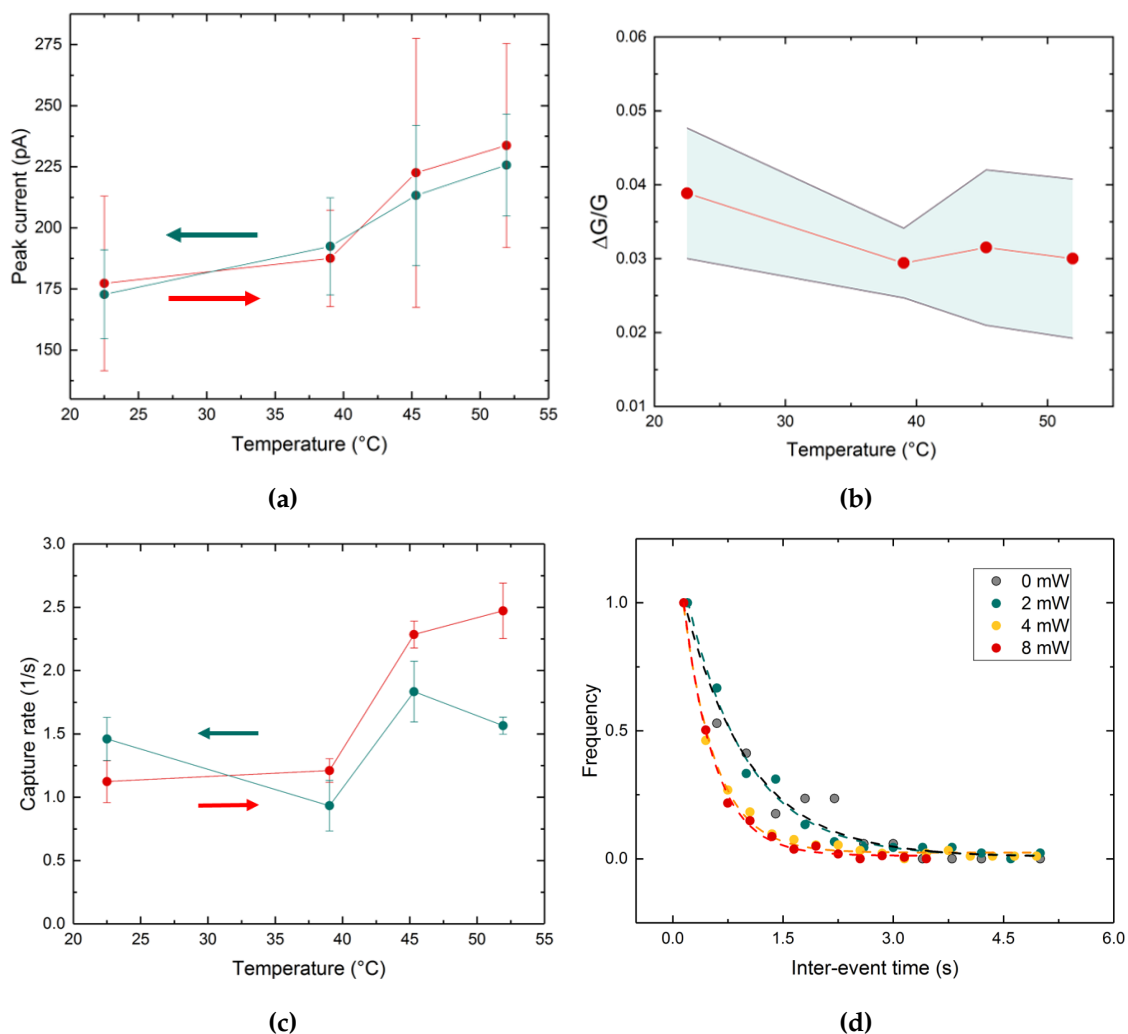


Fig. 4.15 Results illustrating the detailed temperature-induced effects on the translocation dynamics. The experiments were conducted on a AuDBNP at -400 mV, under 632.8 nm laser exposure, for 4 different powers, between 0 mW and 8 mW. (a) Increase in peak current with temperature. (b) The relative conductance blockade $\Delta G/G_0$ remains almost constant, if not slightly decreasing, with temperature. (c) Temperature-induced enhancement of the capture rate. Red curves are associated to the positive-sweep of laser powers (from lowest to highest), blue curves are associated to the corresponding negative-sweep. The error bars are calculated from the exponential fitting of the inter-event time. (d) Exponential fitting of the inter-event time, for different laser powers.

laser powers. As the power of the incoming radiation increases, the exponential decays faster, which results in lower inter-event times, and, thus, a higher event frequency.

To verify the reproducibility of the obtained results, the same experiment was carried out on different AuDBNPs, yielding the same temperature-induced trends. Figure 4.16 summarises the results relative to DNA translocations conducted on a standard AuDBNP, with a bias of -300 mV, and exposed to the 632.8 nm laser, 3

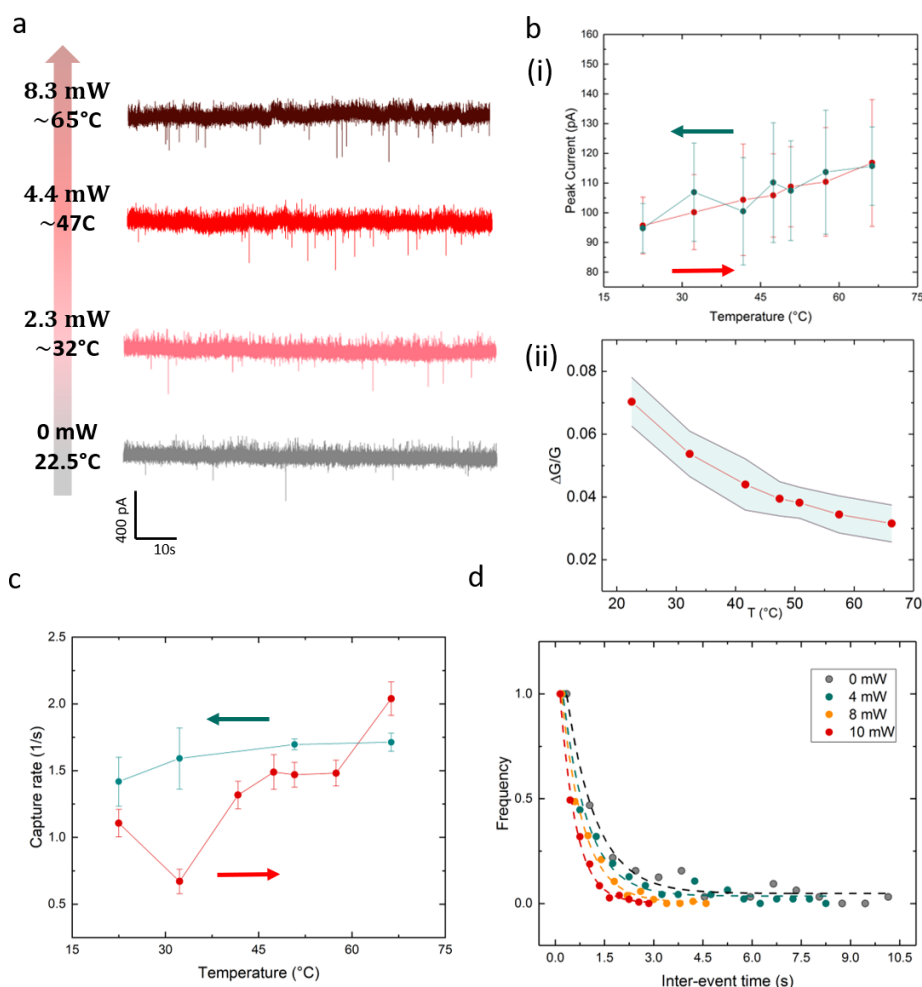


Fig. 4.16 Summary of the results of the temperature induced effects on DNA translocation, on a different AuDBNP. The experiments were conducted at -300 mV, under 632.8 nm laser, for 7 different laser powers. (a) 10s snapshots of the current traces at selected laser powers, confirming event rate increase with temperature. (b)(i) Temperature-induced increase of the Peak current. (ii) Relative conductance blockade $\Delta G/G_0$ as a function of temperature. (c) Temperature-induced effects on the capture rate, showing a clear trend for the positive sweep of laser powers. The altered behaviour of the capture rate during the negative-sweep is due to the long time-scale of the experiment (d) Exponential fitting of the inter-event time, for selected laser powers.

minutes for each of the 7 laser powers (0 mW - 2.3 mW - 4.0 mW - 5.3 mW - 6.3 mW - 8.3 mW - 10.0 mW).

The investigation confirmed what previously stated: temperature enhances the signal amplitude, but not the relative conductance blockade, Figure 4.16b, and it increases the capture rate, Figures 4.16c-d, which passes from $1.1 \pm 0.1 \text{ s}^{-1}$ to $2.0 \pm 0.2 \text{ s}^{-1}$ at the highest laser power/temperature (percentage enhancement $\sim 80 \%$). The altered behaviour of the capture rate during the negative-sweep

is probably due to the long time-scale of the experiment, which leads to a more generalised heating of the pipette's environment, causing the loss of the previously obtained quasi-instantaneous temperature changes. Nonetheless, it is safe to say that regulated localised nanopore heating leads to a reproducible and reversible enhancement of the capture rate, and that the precise temperature modulations obtained via plasmon-excitation enable to control the throughput of the single-molecule translocations.

Strategy 2 - Pulsed Laser Exposure

To further investigate the extent of the controllable capture rate enhancement, Strategy 2 was employed to verify if the system could be used for obtaining an "on-demand" type of throughput modulation. Therefore, the current flowing through an AuDBNP was recorded at a constant bias of -400 mV, and the tip was periodically exposed to a fixed laser power, 4.2 mW. For the results displayed in Figure 4.17, the DNA translocations were recorded for 2 minutes of no illumination, followed by 2 minutes of exposure, and the cycle was repeated two times.

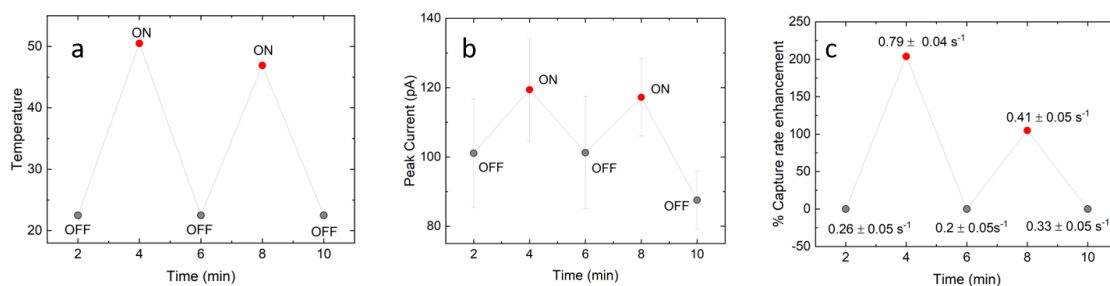


Fig. 4.17 Summary of the preliminary results of the effects of pulsed laser exposure on DNA translocations. The experiments were conducted at -400 mV, switching between 0 mW and 4.2 mW, 2 minutes per cycle. Consistent and reversible control on (a) temperature and (b) Peak current. (c) Controllable Capture Rate relative enhancement.

As Figure 4.17a shows, the change in temperature is highly controllable and reproducible, $\Delta T_1 = 28^\circ\text{C}$ and $\Delta T_2 = 25^\circ\text{C}$, confirming the instantaneous and reversible nature of the laser-induced heating. The enhancement in signal amplitude, depicted in Figure 4.17b, proved to be controllable and reproducible as well. The average capture rates were $0.27 \pm 0.04 \text{ s}^{-1}$ in the off-cycles, and $0.60 \pm 0.05 \text{ s}^{-1}$ in the on-cycles. The values obtained are lower than the corresponding ones resulting from Strategy 1, probably due to inherent differences among pipettes. Nonetheless, the percentage enhancement of the capture rate, reported in Figure 4.17c, is in agreement with previous results, even if not constant among cycles, $\sim 205\%$ in the first and $\sim 105\%$ in the second. Moreover, when the laser was switched

off, the capture rate reverted to similar values, confirming the reversibility of the enhancement.

Due to issues with the set-up, such as a temporarily failure of the eONE amplifier, it was not possible to perform additional successful experiments with Strategy 2. However, the positivity of the results obtained so far suggests that the device fabricated can be employed for on-demand modulations of the throughput.

4.4 Mechanism behind Capture Rate Enhancement

The results described above demonstrate that altering the local environment around the nanopore with precise temperature modulations provides an immediate means of controlling the throughput of the system. A tunable capture rate allows to collect a statistically significant number of translocations in a limited time frame, which is desirable in a number of applications, including sequencing [97]. Moreover, the capture rate enhancement is obtained without altering the dwell time, which is a non-trivial result, also considering that many of the nanopore systems suffer from high translocation velocities [28, 100].

The temperature-induced capture rate increase can be explained considering that heating enhances ion diffusivity around the pore. The reduction in buffer viscosity improves the transport of both electrolyte ions, K^+ and Cl^- , and DNA molecules [85]. Higher DNA diffusion implies a increased probability of entering the capture radius of the pore. Moreover, higher temperatures supply the DNA molecules with a larger kinetic energy, which is likely to favour overcoming the entropic barrier associated to the translocation event [101].

These considerations are corroborated by the geometrical shape of the pipette and the size of the electrodeposited gold bulb. Owing to their conical shape, nanopipettes confine the DNA in a much smaller volume, with less degrees of freedom, compared to the reservoirs of conventional nanopores. In addition to this, the SEM images of the fabricated AuDBNPs have revealed that the gold bulb has a micrometric extension, which means that, even if highly localised, the temperature changes are reasonably uniform on the scale of the DNA molecules confined at the tip of the pipette. In turn, this suggests that no significant temperature gradients are present in the vicinity of the pore opening.

Previous studies have focused on the role of thermal gradients and thermophoresis on the DNA capture dynamics [81, 84, 85, 102], highlighting the competing or complementary roles of electrophoresis and thermophoresis, depending on the electrolyte used. In particular, enhancement in capture rate was

observed in LiCl, characterised by negative thermophoresis, that is, molecules are driven from colder to warmer regions. In this case, the presence of a thermophoretic force driving the DNA molecules towards the warmer pore aids the electrophoretic force, increasing the throughput of the system. On the other hand, the reversed effect was observed in KCl, which exhibits positive thermophoresis, causing DNA molecules to deplete the warmer region around the pore. However, the inherent geometric differences between conventional nanopores and nanopipettes generate diverse heating profiles, which explains the absence of thermophoresis as one of the driving forces leading to the results obtained in this work.

Chapter 5

Conclusion

The project explored the possibility of using local temperature modulations to achieve control over DNA transport through the pore. The promising results confirm the suitability of this approach for obtaining a label-free single-molecule sensor having a tunable throughput. The fabrication of the device proved to be reliable and reproducible, yielding a system with a gold plasmonic feature, capable of responding to laser exposure. The successful integration of laser optics with electrical detection, enabled us to record the ionic current changes induced by the low-noise plasmonic heating at the tip of the gold-modified nanopipettes. These ionic current changes were then used to quantify the local temperature changes, thus enabling the use of the pipette as a nanoscale temperature probe. Exposing the device to different laser powers, between 0 and 16 mW, accurately tuned the extent of heating, yielding temperature variations ranging between 20 °C and 60 °C. These changes were then used to control the throughput of the system during DNA translocations. In particular, higher temperatures in the localised pore environment resulted in a significant capture rate enhancement, mainly due to the improved DNA transport associated to an increased ion diffusion.

The device proposed displays a number of advantages. First of all, the fabrication process is fairly simple and cheap, compared to standard nanopore technology, and, using temperature as the physical parameter to manipulate DNA translocations, avoids more complicated and expensive chemical modifications. This is highly desirable in the prospect of integration with commercial biosensors for point-of-care applications. Moreover, the temperature modulation and capture rate enhancement have proven to be reproducible, reversible, and accurate. The possibility of controlling the capture rate is essential in the development of rapid, versatile, and cost-effective single-molecule sensors.

Chapter 6

Future Research

The results obtained pave the way for different possibilities of future investigations and applications. To achieve a better understanding of the mechanisms that regulate the temperature-induced capture rate enhancement, multiple strategies can be followed. First of all, simulations would contribute toward the achievement of a more detailed characterisation of the temperature profile around the pore and of the forces that govern DNA transport. To quantify the contribution of thermophoretic forces, current-clamp experiments could measure the potential arising across the pore upon laser exposure. In addition to this, varying a few elements of the setup used, such as replacing KCl with LiCl, or performing translocations from the outside to the inside of the pipette, could bring to a deeper understanding of the roles of thermophoresis and ion diffusion.

Confirming the on-demand throughput enhancement obtained with pulsed laser exposure, could lead to on-demand delivery of analytes, crucial in targeted drug delivery applications. Alternatively, the significant temperature variations that arise in the nanopore environment could be used to characterise the conformational changes that occur in analytes due heating, and how the binding properties of aptamers and DNA-carriers respond to altered temperature conditions. Finally, the versatility of the fabricated device allows to integrate several types of surface functionalisation on the gold tip. For example, self-assembled attachment of thiolated aptamers would provide a selective detection of target molecules, due to specific binding. The gold bulb at the tip could also be equipped with temperature-sensitive polymers, which would introduce additional gating functions in the nanopore.

References

- [1] C. Nicolini, M. Adami, F. Antolini, F. Beltram, and M. Sartore, "Biosensors : a step to bioelectronics," *Physics World*, vol. 5, no. 5, p. 30, 1992.
- [2] A. P. F. Turner, "Biosensors: sense and sensibility," *Chemical Society Reviews*, vol. 42, no. 8, p. 3184, 2013.
- [3] B. N. Miles, A. P. Ivanov, K. A. Wilson, F. Doğan, D. Japrun, and J. B. Edel, "Single molecule sensing with solid-state nanopores: novel materials, methods, and applications," *Chem. Soc. Rev.*, vol. 42, no. 1, pp. 15–28, 2013.
- [4] M. L. Sin, K. E. Mach, P. K. Wong, and J. C. Liao, "Advances and challenges in biosensor-based diagnosis of infectious diseases," *Expert Review of Molecular Diagnostics*, vol. 14, pp. 225–244, mar 2014.
- [5] J. Y. Y. Sze, A. P. Ivanov, A. E. G. Cass, and J. B. Edel, "Single molecule multiplexed nanopore protein screening in human serum using aptamer modified DNA carriers," *Nature Communications*, vol. 8, p. 1552, dec 2017.
- [6] I. Tothill and Z. Altintas, "Molecular biosensors: promising new tools for early detection of cancer," *Nanobiosensors in Disease Diagnosis*, vol. 4, p. 1, jan 2015.
- [7] S. Mousa, "Biosensors: the new wave in cancer diagnosis," *Nanotechnology, Science and Applications*, vol. 4, p. 1, dec 2010.
- [8] J.-H. Oh and J.-S. Lee, "Designed Hybridization Properties of DNA–Gold Nanoparticle Conjugates for the Ultrasensitive Detection of a Single-Base Mutation in the Breast Cancer Gene BRCA1," *Analytical Chemistry*, vol. 83, pp. 7364–7370, oct 2011.
- [9] J. Kong, J. Zhu, and U. F. Keyser, "Single molecule based SNP detection using designed DNA carriers and solid-state nanopores," *Chemical Communications*, vol. 53, no. 2, pp. 436–439, 2017.
- [10] J. Vidic, M. Manzano, C.-M. Chang, and N. Jaffrezic-Renault, "Advanced biosensors for detection of pathogens related to livestock and poultry," *Veterinary Research*, vol. 48, p. 11, dec 2017.
- [11] C. F. Fronczek and J.-Y. Yoon, "Biosensors for Monitoring Airborne Pathogens," *Journal of Laboratory Automation*, vol. 20, pp. 390–410, aug 2015.
- [12] J. J. Gooding and K. Gaus, "Single-Molecule Sensors: Challenges and Opportunities for Quantitative Analysis," *Angewandte Chemie International Edition*, vol. 55, pp. 11354–11366, sep 2016.

- [13] D. R. Walt, "Optical Methods for Single Molecule Detection and Analysis," *Analytical Chemistry*, vol. 85, pp. 1258–1263, feb 2013.
- [14] B. M. Venkatesan and R. Bashir, "Nanopore sensors for nucleic acid analysis," *Nature Nanotechnology*, vol. 6, pp. 615–624, oct 2011.
- [15] S. Shashkova and M. C. Leake, "Single-molecule fluorescence microscopy review: shedding new light on old problems," *Bioscience Reports*, vol. 37, p. BSR20170031, aug 2017.
- [16] M. F. Juette, D. S. Terry, M. R. Wasserman, Z. Zhou, R. B. Altman, Q. Zheng, and S. C. Blanchard, "The bright future of single-molecule fluorescence imaging," *Current Opinion in Chemical Biology*, vol. 20, pp. 103–111, jun 2014.
- [17] Y. Gao, L. Deng, Q. Yan, Y. Gao, Z. Wu, J. Cai, D. Ji, G. Li, P. Wu, H. Jin, L. Zhao, S. Liu, L. Ge, M. W. Deem, and J. He, "Single molecule targeted sequencing for cancer gene mutation detection," *Scientific Reports*, vol. 6, p. 26110, sep 2016.
- [18] E. M. Kudalkar, T. N. Davis, and C. L. Asbury, "Single-Molecule Total Internal Reflection Fluorescence Microscopy," *Cold Spring Harbor Protocols*, vol. 2016, p. pdb.top077800, may 2016.
- [19] O. N. Assad, T. Gilboa, J. Spitzberg, M. Juhasz, E. Weinhold, and A. Meller, "Light-Enhancing Plasmonic-Nanopore Biosensor for Superior Single-Molecule Detection," *Advanced Materials*, vol. 29, p. 1605442, mar 2017.
- [20] M. P. Cecchini, A. Wiener, V. A. Turek, H. Chon, S. Lee, A. P. Ivanov, D. W. McComb, J. Choo, T. Albrecht, S. A. Maier, and J. B. Edel, "Rapid Ultrasensitive Single Particle Surface-Enhanced Raman Spectroscopy Using Metallic Nanopores," *Nano Letters*, vol. 13, pp. 4602–4609, oct 2013.
- [21] K. J. Freedman, C. R. Crick, P. Albella, A. Barik, A. P. Ivanov, S. A. Maier, S.-H. Oh, and J. B. Edel, "On-Demand Surface- and Tip-Enhanced Raman Spectroscopy Using Dielectrophoretic Trapping and Nanopore Sensing," *ACS Photonics*, vol. 3, pp. 1036–1044, jun 2016.
- [22] E. A. Vitol, Z. Orynbayeva, M. J. Bouchard, J. Azizkhan-Clifford, G. Friedman, and Y. Gogotsi, "In Situ Intracellular Spectroscopy with Surface Enhanced Raman Spectroscopy (SERS)-Enabled Nanopipettes," *ACS Nano*, vol. 3, pp. 3529–3536, nov 2009.
- [23] K. C. Neuman and A. Nagy, "Single-molecule force spectroscopy: optical tweezers, magnetic tweezers and atomic force microscopy," *Nature Methods*, vol. 5, pp. 491–505, jun 2008.
- [24] F. M. Fazal, D. J. Koslover, B. F. Luisi, and S. M. Block, "Direct observation of processive exoribonuclease motion using optical tweezers," *Proceedings of the National Academy of Sciences*, vol. 112, pp. 15101–15106, dec 2015.
- [25] M. Petersen, J. Schwab, S. Gruber, N. Blaser, M. Schomaker, and M. van der Laan, "Targeted Maximum Likelihood Estimation for Dynamic and Static Longitudinal Marginal Structural Working Models," *Journal of Causal Inference*, vol. 2, pp. 147–185, jan 2014.

- [26] K. Iwata, S. Yamazaki, P. Mutombo, P. Hapala, M. Ondráček, P. Jelínek, and Y. Sugimoto, "Chemical structure imaging of a single molecule by atomic force microscopy at room temperature," *Nature Communications*, vol. 6, p. 7766, dec 2015.
- [27] G. Sirinakis, Y. Ren, Y. Gao, Z. Xi, and Y. Zhang, "Combined versatile high-resolution optical tweezers and single-molecule fluorescence microscopy," *Review of Scientific Instruments*, vol. 83, p. 093708, sep 2012.
- [28] M. Wanunu, "Nanopores: A journey towards DNA sequencing," *Physics of Life Reviews*, vol. 9, pp. 125–158, jun 2012.
- [29] D. G. Haywood, A. Saha-Shah, L. A. Baker, and S. C. Jacobson, "Fundamental Studies of Nanofluidics: Nanopores, Nanochannels, and Nanopipets," *Analytical Chemistry*, vol. 87, pp. 172–187, jan 2015.
- [30] J. J. Kasianowicz, E. Brandin, D. Branton, and D. W. Deamer, "Characterization of individual polynucleotide molecules using a membrane channel," *Proceedings of the National Academy of Sciences*, vol. 93, pp. 13770–13773, nov 1996.
- [31] M. J. Kim, M. Wanunu, D. C. Bell, and A. Meller, "Rapid Fabrication of Uniformly Sized Nanopores and Nanopore Arrays for Parallel DNA Analysis," *Advanced Materials*, vol. 18, pp. 3149–3153, dec 2006.
- [32] M. Muthukumar, "Mechanism of DNA Transport Through Pores," *Annual Review of Biophysics and Biomolecular Structure*, vol. 36, pp. 435–450, jun 2007.
- [33] J.-F. Masson, J. Breault-Turcot, R. Faid, H.-P. Poirier-Richard, H. Yockell-Lelièvre, F. Lussier, and J. P. Spatz, "Plasmonic Nanopipette Biosensor," *Analytical Chemistry*, vol. 86, pp. 8998–9005, sep 2014.
- [34] A. Squires, T. Gilboa, C. Torfstein, N. Varongchayakul, and A. Meller, "Single-Molecule Characterization of DNA–Protein Interactions Using Nanopore Biosensors," in *Methods in Enzymology*, vol. 582, pp. 353–385, Elsevier Inc., 1 ed., 2017.
- [35] S. Agah, M. Zheng, M. Pasquali, and A. B. Kolomeisky, "DNA sequencing by nanopores: advances and challenges," *Journal of Physics D: Applied Physics*, vol. 49, p. 413001, oct 2016.
- [36] S. Carson and M. Wanunu, "Challenges in DNA motion control and sequence readout using nanopore devices," *Nanotechnology*, vol. 26, p. 074004, feb 2015.
- [37] R. M. Manara, E. Jayne Wallace, and S. Khalid, "DNA sequencing with MspA: Molecular Dynamics simulations reveal free-energy differences between sequencing and non-sequencing mutants," *Scientific Reports*, vol. 5, p. 12783, oct 2015.
- [38] J. Shendure, S. Balasubramanian, G. M. Church, W. Gilbert, J. Rogers, J. A. Schloss, and R. H. Waterston, "DNA sequencing at 40: past, present and future," *Nature*, vol. 550, pp. 345–353, oct 2017.
- [39] J. F. Siqueira, A. F. Fouad, and I. N. Rôças, "Pyrosequencing as a tool for better understanding of human microbiomes," *Journal of Oral Microbiology*, vol. 4, p. 10743, jan 2012.

- [40] M. Akeson, D. Branton, J. J. Kasianowicz, E. Brandin, and D. W. Deamer, "Microsecond Time-Scale Discrimination Among Polycytidylic Acid, Polyadenylic Acid, and Polyuridylic Acid as Homopolymers or as Segments Within Single RNA Molecules," *Biophysical Journal*, vol. 77, pp. 3227–3233, dec 1999.
- [41] F. Haque, J. Li, H.-C. Wu, X.-J. Liang, and P. Guo, "Solid-state and biological nanopore for real-time sensing of single chemical and sequencing of DNA," *Nano Today*, vol. 8, pp. 56–74, feb 2013.
- [42] A. Meller and D. Branton, "Single molecule measurements of DNA transport through a nanopore," *ELECTROPHORESIS*, vol. 23, pp. 2583–2591, aug 2002.
- [43] Y.-L. Ying, C. Cao, and Y.-T. Long, "Single molecule analysis by biological nanopore sensors," *The Analyst*, vol. 139, no. 16, pp. 3826–3835, 2014.
- [44] J. Clarke, H.-C. Wu, L. Jayasinghe, A. Patel, S. Reid, and H. Bayley, "Continuous base identification for single-molecule nanopore DNA sequencing," *Nature Nanotechnology*, vol. 4, pp. 265–270, apr 2009.
- [45] J. B. Edel and T. Albrecht, *Engineered Nanopores for Bioanalytical Applications*. Elsevier, 2013.
- [46] Z. Tang, D. Zhang, W. Cui, H. Zhang, W. Pang, and X. Duan, "Fabrications, Applications and Challenges of Solid-State Nanopores: A Mini Review," *Nanomaterials and Nanotechnology*, vol. 6, p. 35, jan 2016.
- [47] X. Gong, A. V. Patil, A. P. Ivanov, Q. Kong, T. Gibb, F. Dogan, A. J. DeMello, and J. B. Edel, "Label-Free In-Flow Detection of Single DNA Molecules using Glass Nanopipettes," *Analytical Chemistry*, vol. 86, pp. 835–841, jan 2014.
- [48] G. A. T. Chansin, R. Mulero, J. Hong, M. J. Kim, A. J. DeMello, and J. B. Edel, "Single-Molecule Spectroscopy Using Nanoporous Membranes," *Nano Letters*, vol. 7, pp. 2901–2906, sep 2007.
- [49] G. V. Soni, A. Singer, Z. Yu, Y. Sun, B. McNally, and A. Meller, "Synchronous optical and electrical detection of biomolecules traversing through solid-state nanopores," *Review of Scientific Instruments*, vol. 81, p. 014301, jan 2010.
- [50] A. P. Ivanov, E. Instuli, C. M. McGilvery, G. Baldwin, D. W. McComb, T. Albrecht, and J. B. Edel, "DNA Tunneling Detector Embedded in a Nanopore," *Nano Letters*, vol. 11, pp. 279–285, jan 2011.
- [51] H. Peng and X. S. Ling, "Reverse DNA translocation through a solid-state nanopore by magnetic tweezers," *Nanotechnology*, vol. 20, p. 185101, may 2009.
- [52] A. J. Storm, J. H. Chen, X. S. Ling, H. W. Zandbergen, and C. Dekker, "Fabrication of solid-state nanopores with single-nanometre precision," *Nature Materials*, vol. 2, pp. 537–540, aug 2003.
- [53] J. Gierak, A. Madouri, A. Bianco, E. Bourhis, G. Patriarche, C. Ulysse, D. Lucot, X. Lafosse, L. Auvray, L. Bruchhaus, and R. Jede, "Sub-5nm FIB direct patterning of nanodevices," *Microelectronic Engineering*, vol. 84, pp. 779–783, may 2007.

- [54] P. Chen, T. Mitsui, D. B. Farmer, J. Golovchenko, R. G. Gordon, and D. Branton, "Atomic Layer Deposition to Fine-Tune the Surface Properties and Diameters of Fabricated Nanopores," *Nano Letters*, vol. 4, pp. 1333–1337, jul 2004.
- [55] S. Garaj, W. Hubbard, A. Reina, J. Kong, D. Branton, and J. A. Golovchenko, "Graphene as a subnanometre trans-electrode membrane," *Nature*, vol. 467, pp. 190–193, sep 2010.
- [56] J. Y. Y. Sze, S. Kumar, A. P. Ivanov, S.-H. Oh, and J. B. Edel, "Fine tuning of nanopipettes using atomic layer deposition for single molecule sensing," *The Analyst*, vol. 140, no. 14, pp. 4828–4834, 2015.
- [57] J. Nilsson, J. R. I. Lee, T. V. Ratto, and S. E. Létant, "Localized Functionalization of Single Nanopores," *Advanced Materials*, vol. 18, pp. 427–431, feb 2006.
- [58] V. Mussi, P. Fanzio, G. Firpo, L. Repetto, and U. Valbusa, "Size and functional tuning of solid state nanopores by chemical functionalization," *Nanotechnology*, vol. 23, p. 435301, nov 2012.
- [59] A. Rutkowska, K. Freedman, J. Skalkowska, M. J. Kim, J. B. Edel, and T. Albrecht, "Electrodeposition and Bipolar Effects in Metallized Nanopores and Their Use in the Detection of Insulin," *Analytical Chemistry*, vol. 87, pp. 2337–2344, feb 2015.
- [60] M. Ayub, A. Ivanov, E. Instuli, M. Cecchini, G. Chansin, C. McGilvery, J. Hong, G. Baldwin, D. McComb, J. B. Edel, and T. Albrecht, "Nanopore/electrode structures for single-molecule biosensing," *Electrochimica Acta*, vol. 55, pp. 8237–8243, nov 2010.
- [61] P. Actis, A. C. Mak, and N. Pourmand, "Functionalized nanopipettes: toward label-free, single cell biosensors," *Bioanalytical Reviews*, vol. 1, pp. 177–185, aug 2010.
- [62] C. R. Crick, J. Y. Y. Sze, M. Rosillo-Lopez, C. G. Salzmänn, and J. B. Edel, "Selectively Sized Graphene-Based Nanopores for in Situ Single Molecule Sensing," *ACS Applied Materials & Interfaces*, vol. 7, pp. 18188–18194, aug 2015.
- [63] A. P. Ivanov, P. Actis, P. Jönsson, D. Klenerman, Y. Korchev, and J. B. Edel, "On-Demand Delivery of Single DNA Molecules Using Nanopipets," *ACS Nano*, vol. 9, pp. 3587–3595, apr 2015.
- [64] M. Wanunu, J. Sutin, B. McNally, A. Chow, and A. Meller, "DNA Translocation Governed by Interactions with Solid-State Nanopores," *Biophysical Journal*, vol. 95, pp. 4716–4725, nov 2008.
- [65] K. J. Freedman, L. M. Otto, A. P. Ivanov, A. Barik, S.-H. Oh, and J. B. Edel, "Nanopore sensing at ultra-low concentrations using single-molecule dielectrophoretic trapping," *Nature Communications*, vol. 7, p. 10217, jan 2016.
- [66] P. Cadinu, G. Campolo, S. Pud, W. Yang, J. B. Edel, C. Dekker, and A. P. Ivanov, "Double Barrel Nanopores as a New Tool for Controlling Single-Molecule Transport," *Nano Letters*, vol. 18, pp. 2738–2745, apr 2018.

- [67] P. Cadinu, B. Paulose Nadappuram, D. J. Lee, J. Y. Y. Sze, G. Campolo, Y. Zhang, A. Shevchuk, S. Ladame, T. Albrecht, Y. Korchev, A. P. Ivanov, and J. B. Edel, "Single Molecule Trapping and Sensing Using Dual Nanopores Separated by a Zeptoliter Nanobridge," *Nano Letters*, vol. 17, pp. 6376–6384, oct 2017.
- [68] Y. Takahashi, A. I. Shevchuk, P. Novak, Y. Zhang, N. Ebejer, J. V. Macpherson, P. R. Unwin, A. J. Pollard, D. Roy, C. A. Clifford, H. Shiku, T. Matsue, D. Klenerman, and Y. E. Korchev, "Multifunctional Nanoprobes for Nanoscale Chemical Imaging and Localized Chemical Delivery at Surfaces and Interfaces," *Angewandte Chemie International Edition*, vol. 50, pp. 9638–9642, oct 2011.
- [69] K. McKelvey, B. P. Nadappuram, P. Actis, Y. Takahashi, Y. E. Korchev, T. Matsue, C. Robinson, and P. R. Unwin, "Fabrication, Characterization, and Functionalization of Dual Carbon Electrodes as Probes for Scanning Electrochemical Microscopy (SECM)," *Analytical Chemistry*, vol. 85, pp. 7519–7526, aug 2013.
- [70] C. R. Crick, P. Albella, H.-J. Kim, A. P. Ivanov, K.-B. Kim, S. A. Maier, and J. B. Edel, "Low-Noise Plasmonic Nanopore Biosensors for Single Molecule Detection at Elevated Temperatures," *ACS Photonics*, vol. 4, pp. 2835–2842, nov 2017.
- [71] W. Shi, N. Sa, R. Thakar, and L. A. Baker, "Nanopipette delivery: influence of surface charge," *The Analyst*, vol. 140, no. 14, pp. 4835–4842, 2015.
- [72] S. Umehara, M. Karhanek, R. W. Davis, and N. Pourmand, "Label-free biosensing with functionalized nanopipette probes," *Proceedings of the National Academy of Sciences*, vol. 106, pp. 4611–4616, mar 2009.
- [73] Y. Fu, H. Tokuhisa, and L. A. Baker, "Nanopore DNA sensors based on dendrimer-modified nanopipettes," *Chemical Communications*, no. 32, p. 4877, 2009.
- [74] D. Fologea, J. Uplinger, B. Thomas, D. S. McNabb, and J. Li, "Slowing DNA Translocation in a Solid-State Nanopore," *Nano Letters*, vol. 5, pp. 1734–1737, sep 2005.
- [75] M. Wanunu, W. Morrison, Y. Rabin, A. Y. Grosberg, and A. Meller, "Electrostatic focusing of unlabelled DNA into nanoscale pores using a salt gradient," *Nature Nanotechnology*, vol. 5, pp. 160–165, feb 2010.
- [76] Y. Zhang, G. Wu, W. Si, J. Ma, Z. Yuan, X. Xie, L. Liu, J. Sha, D. Li, and Y. Chen, "Ionic current modulation from DNA translocation through nanopores under high ionic strength and concentration gradients," *Nanoscale*, vol. 9, no. 2, pp. 930–939, 2017.
- [77] R. M. M. Smeets, U. F. Keyser, N. H. Dekker, and C. Dekker, "Noise in solid-state nanopores," *Proceedings of the National Academy of Sciences*, vol. 105, pp. 417–421, jan 2008.
- [78] B. Lu, D. P. Hoogerheide, Q. Zhao, H. Zhang, Z. Tang, D. Yu, and J. A. Golovchenko, "Pressure-Controlled Motion of Single Polymers through Solid-State Nanopores," *Nano Letters*, vol. 13, pp. 3048–3052, jul 2013.

- [79] D. V. Verschueren, M. P. Jonsson, and C. Dekker, "Temperature dependence of DNA translocations through solid-state nanopores," *Nanotechnology*, vol. 26, p. 234004, jun 2015.
- [80] C. R. Crick, P. Albella, B. Ng, A. P. Ivanov, T. Roschuk, M. P. Cecchini, F. Bresme, S. A. Maier, and J. B. Edel, "Precise Attoliter Temperature Control of Nanopore Sensors Using a Nanoplasmonic Bullseye," *Nano Letters*, vol. 15, pp. 553–559, jan 2015.
- [81] F. Nicoli, D. Verschueren, M. Klein, C. Dekker, and M. P. Jonsson, "DNA Translocations through Solid-State Plasmonic Nanopores," *Nano Letters*, vol. 14, pp. 6917–6925, dec 2014.
- [82] M. P. Jonsson and C. Dekker, "Plasmonic Nanopore for Electrical Profiling of Optical Intensity Landscapes," *Nano Letters*, vol. 13, pp. 1029–1033, mar 2013.
- [83] S. Pud, D. Verschueren, N. Vukovic, C. Plesa, M. P. Jonsson, and C. Dekker, "Self-Aligned Plasmonic Nanopores by Optically Controlled Dielectric Breakdown," *Nano Letters*, vol. 15, pp. 7112–7117, oct 2015.
- [84] H. Yamazaki, R. Hu, R. Y. Henley, J. Halman, K. A. Afonin, D. Yu, Q. Zhao, and M. Wanunu, "Label-Free Single-Molecule Thermoscopy Using a Laser-Heated Nanopore," *Nano Letters*, vol. 17, pp. 7067–7074, nov 2017.
- [85] M. Zhang, C. Ngampeerapong, D. Redin, A. Ahmadian, I. Sychugov, and J. Linnros, "Thermophoresis-Controlled Size-Dependent DNA Translocation through an Array of Nanopores," *ACS Nano*, vol. 12, pp. 4574–4582, may 2018.
- [86] B. P. Nadappuram, K. McKelvey, R. Al Botros, A. W. Colburn, and P. R. Unwin, "Fabrication and Characterization of Dual Function Nanoscale pH-Scanning Ion Conductance Microscopy (SICM) Probes for High Resolution pH Mapping," *Analytical Chemistry*, vol. 85, pp. 8070–8074, sep 2013.
- [87] P. Actis, S. Tokar, J. Clausmeyer, B. Babakinejad, S. Mikhaleva, R. Cornut, Y. Takahashi, A. López Córdoba, P. Novak, A. I. Shevchuck, J. A. Dougan, S. G. Kazarian, P. V. Gorelkin, A. S. Erofeev, I. V. Yaminsky, P. R. Unwin, W. Schuhmann, D. Klenerman, D. A. Rusakov, E. V. Sviderskaya, and Y. E. Korchev, "Electrochemical Nanoprobes for Single-Cell Analysis," *ACS Nano*, vol. 8, pp. 875–884, jan 2014.
- [88] M. Ayub, A. Ivanov, J. Hong, P. Kuhn, E. Instuli, J. B. Edel, and T. Albrecht, "Precise electrochemical fabrication of sub-20 nm solid-state nanopores for single-molecule biosensing," *Journal of Physics: Condensed Matter*, vol. 22, p. 454128, nov 2010.
- [89] L. Xue, *A Single-Molecule Switchable Sensing Tool by Integrating Dual-Barrel Nanopipettes with Field-Effect Transistors*. PhD thesis, Imperial College London, 2016.
- [90] A. M. Smith, A. A. Lee, and S. Perkin, "The Electrostatic Screening Length in Concentrated Electrolytes Increases with Concentration," *The Journal of Physical Chemistry Letters*, vol. 7, pp. 2157–2163, jun 2016.

- [91] R. H. Shreiner and K. W. Pratt, "Primary Standards and Standard Reference Materials for Electrolytic Conductivity Standard Reference Materials : Primary Standards and Standard Reference Materials for Electrolytic Conductivity," *NIST Special Publication 260-142*, p. 9, 2004.
- [92] A. P. Ivanov, P. Actis, P. Jönsson, D. Klenerman, Y. Korchev, and J. B. Edel, "On-Demand Delivery of Single DNA Molecules Using Nanopipets," *ACS Nano*, vol. 9, pp. 3587–3595, apr 2015.
- [93] T. R. Gibb, A. P. Ivanov, J. B. Edel, and T. Albrecht, "Single Molecule Ionic Current Sensing in Segmented Flow Microfluidics," *Analytical Chemistry*, vol. 86, pp. 1864–1871, feb 2014.
- [94] Z. Roelen, J. A. Bustamante, A. Carlsen, A. Baker-Murray, and V. Tabard-Cossa, "Instrumentation for low noise nanopore-based ionic current recording under laser illumination," *Review of Scientific Instruments*, vol. 89, p. 015007, jan 2018.
- [95] C. Lefrou and R. Cornut, "Analytical Expressions for Quantitative Scanning Electrochemical Microscopy (SECM)," *ChemPhysChem*, vol. 11, pp. 547–556, feb 2010.
- [96] Z. Yu, T. E. McKnight, M. N. Ericson, A. V. Melechko, M. L. Simpson, and B. Morrison, "Vertically Aligned Carbon Nanofiber Arrays Record Electrophysiological Signals from Hippocampal Slices," *Nano Letters*, vol. 7, pp. 2188–2195, aug 2007.
- [97] Y. He, M. Tsutsui, R. H. Scheicher, F. Bai, M. Taniguchi, and T. Kawai, "Thermophoretic Manipulation of DNA Translocation through Nanopores," *ACS Nano*, vol. 7, pp. 538–546, jan 2013.
- [98] A. Y. Grosberg and Y. Rabin, "DNA capture into a nanopore: Interplay of diffusion and electrohydrodynamics," *The Journal of Chemical Physics*, vol. 133, p. 165102, oct 2010.
- [99] M. Belkin and A. Aksimentiev, "Molecular Dynamics Simulation of DNA Capture and Transport in Heated Nanopores," *ACS Applied Materials & Interfaces*, vol. 8, pp. 12599–12608, may 2016.
- [100] S. W. Kowalczyk, D. B. Wells, A. Aksimentiev, and C. Dekker, "Slowing down DNA Translocation through a Nanopore in Lithium Chloride," *Nano Letters*, vol. 12, pp. 1038–1044, feb 2012.
- [101] M. Belkin, C. Maffeo, D. B. Wells, and A. Aksimentiev, "Stretching and Controlled Motion of Single-Stranded DNA in Locally Heated Solid-State Nanopores," *ACS Nano*, vol. 7, pp. 6816–6824, aug 2013.
- [102] M. Belkin, S.-H. Chao, M. P. Jonsson, C. Dekker, and A. Aksimentiev, "Plasmonic Nanopores for Trapping, Controlling Displacement, and Sequencing of DNA," *ACS Nano*, vol. 9, pp. 10598–10611, nov 2015.